MinEx CRC Limited
26 Dick Perry Avenue, Kensington, WA, 6151
PO Box 1130, Bentley, WA, 6102, Australia
admin@minexcrc.com.au

MinEx CRC
ABN: 66 625 533 913

MinEx CRC provides financial support to the value of $1K to promote Honours and Masters by Coursework projects that are aligned with the mission of MinEx CRC and to encourage young researchers toward a career in mineral exploration research. Projects are not restricted to MinEx CRC Participants and Affiliates.

Please note that the content of this thesis has not been subjected to peer-review and subsequent corrections.

Australian Government
Department of Industry, Science and Resources

Cooperative Research Centres Program

Copper isotopes tracing metal transport and concentration at the Whakaari embryonic porphyry copper deposit

Thesis submitted in accordance with the requirements of the University of Adelaide for an Honours Degree in Geology

Jarred Thomas Tilby
November 2023

COPPER ISOTOPES TRACING METAL TRANSPORT AND CONCENTRATION AT THE WHAKAARI/WHITE ISLAND EMBRYONIC PORPHYRY COPPER DEPOSIT

COPPER ISOTOPES AT WHAKAARI

ABSTRACT

The genesis of porphyry copper deposits (PCD) is difficult to study due volcanic destruction and intense alteration. The stratovolcano Whakaari, in New Zealand, provides a modern analogue of an embryonic PCD, with early-stage transport and concentration mechanisms ongoing and recorded in the rock record. Copper isotope fractionation is heavily influenced by changeable REDOX conditions and fluid interactions, which are thought to be primary processes in PCD formation; copper isotopes present as a powerful tracer of formation mechanisms. A suite of lava samples and crater lake sediments are analysed for comparison between igneous processes and a primary hydrothermal endmember. This study uses whole rock major and trace element analysis, copper isotope analysis and petrography. δ^{65}Cu values range between -0.11‰ and 0.59‰, with all but one sample being considered isotopically heavy. The range of values are not representative of a mantle source, and indicate that there are processes affecting copper transport outside of magma ascent. δ^{65}Cu values show insignificant correlation between rock evolution, and do not conform to Rayleigh fractionation modelling that would be indicative of transport via igneous processes. Values are consistent with those expected of sulphide minerals deposited from magmatic brines, and are observed in several of the lava samples and sediments. Cu isotope analysis furthers our understanding of metal transport processes at Whakaari, and can be applied to broader understanding of porphyry copper genesis. Analysis of additional hydrothermal endmembers, combined with Sn, Fe and Zn isotopes to investigate REDOX conditions, will supplement the findings presented in this study.

Keywords

Copper isotopes, Whakaari/White Island, Porphyry copper deposits (PCD), Metal transport, Magmatic fluids

TABLE OF CONTENTS

LIST OF FIGURES AND TABLES

INTRODUCTION

As the global economy shifts away from fossil fuels, humanity will become ever more reliant on critical metals such as copper. With rising demand for electric vehicles, wind farms and large-scale batteries, global copper demand is forecast for a dramatic increase by 2050 (Schipper et al. 2018). Porphyry copper deposits (PCDs) currently account for two thirds of the global supply of copper (Doebrich 2009), and large high-grade deposits are becoming harder to find. Research into the genesis of porphyry copper systems may allow for new ideas, such as in-situ recovery of metal rich brines (Blundy et al. 2021), to meet the supply deficit.

The issue when studying porphyry copper deposits, is that globally, there are very few deposits in comparison to similarly aged hydrothermal deposits. The lack of preservation throughout history due to related orogenesis, consequential erosion, and hydrothermal overprinting makes genesis studies difficult (Seedorff et al. 2005). Therefore, it can be seen that extraordinary circumstances are needed to create an ore-forming hydrothermal system. These processes are hard to deduce from extinct and historically limited examples (Lee and Tang 2020). Whakaari is considered to be an embryonic porphyry copper system (Rapien et al. 2005, Hedenquist et al. 1993), the only known modern analogue of such systems, proving great opportunity to better constrain processes and timeframes associated in forming PCDs. In this study, the transport and concentration of metals via interactions between magmatic and hydrothermal processes is investigated. In typical volcanism, the transport of material is conducted via magma ascent, fractional crystallisation and magmatic fluids, however, porphyry copper deposits are thought to require additional processes to accommodate such a high degree of metal concentration (Lee and Tang 2020, Blundy et al. 2021, Jenner et al. 2010). Copper isotopes are powerful tracers of such processes, as they are not strongly fractionated by high temperature processes such as crystallisation or melting, but are affected by fluid and volatile interactions (Moynier et al. 2017). Previous research has focused on copper fractionation in low temperature processes effecting existing ore bodies, such as supergene enrichment, weathering, and oxidation (Markl et al. 2006, Larson et al. 2003, Maher and Larson 2007). This study uses whole rock major and trace element chemistry and Cu isotope analyses to investigate metal movement at Whakaari to better understand the genesis of porphyry copper deposits (PCDs).

Copper Isotopes

Copper (Cu) is a red-brown transition metal and exists as Cu (0) native copper, copper (I) in sulphides and Cu(II) product of oxidation (Moynier et al. 2017). Copper has two stable isotopes, ^{63}Cu and ^{65}Cu, and have natural abundances of 0.6915% and 0.3085% respectively (Meija et al. 2016); their isotopic ratio is expressed as δ^{65}Cu (relative to a standard reference material – NIST 976) (equation 1). Copper isotope fractionation occurs in changeable REDOX conditions, most readily during fluid/volatile interactions and at low temperatures (Larson et al. 2003, Markl et al. 2006). When fractionating, ^{63}Cu changes phase more readily, leaving behind a heavy ($>^{65}$Cu) residue. Conversely, there is little fractionation of copper isotopes during high temperature processes such as fractional crystallisation, which is thought to be attributed to the highly chalcophile and incompatible nature of the element (Liu et al. 2014, Moynier et al. 2017, Hsu et al. 2017). Isotopes can be fractionated at equilibrium with their system, e.g., a closed mineral/magma system, or kinetically, via physical separation of the species, e.g., hydrothermal reworking. As a result of its unidirectional nature, kinetic fractionation tends to yield larger ratios than equilibrium fractionations in the same low temperature environment (Kendall and McDonnell 1998). Fractionation at high temperature allows for isotopes to change phase more readily, and results in only small changes from the source δ^{65}Cu value.

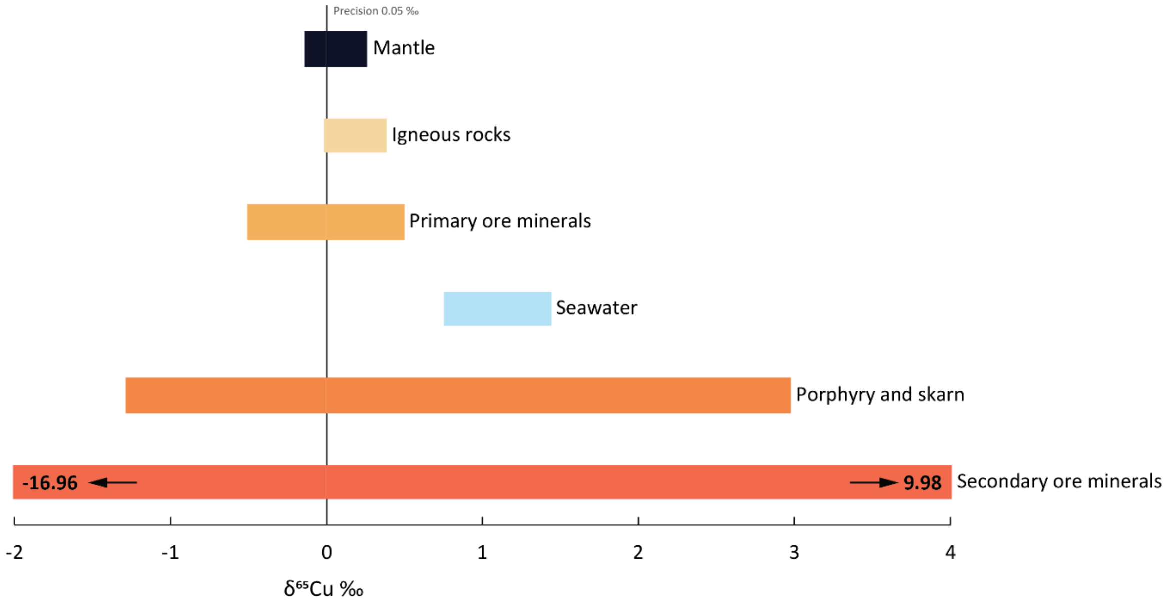

Figure 1: Schematic of copper fractionation in various geological settings. Highlighting how mantle values show little deviation from zero. δ65Cu values are from Liu et al. (2015), Liu et al. (2014), Maher and Larson (2007), Mathur et al. (2009) and Vance et al. (2008).

Figure 1 shows the broad scope of δ^{65}Cu signatures relevant to PCD's, ranging from very little deviation (mantle, fresh igneous rocks), to large variations seen in secondary minerals reworked by hydrothermal fluids at low temperatures. Primary ore signatures show minimal variation; Guo et al. (2020) theorises that two-phase fluids in PCDs have separate light (vapour) and heavy (brine) signatures that affect primary ore deposition. Primary ore minerals that have significant variation in δ^{65}Cu values are seen as having been remobilised from a previous, already fractionated source (Markl et al. 2006).

Porphyry Copper Deposits

Porphyry Copper Deposits are large, intrusive, igneous ore bodies (10-100km^3) that host the majority of the global copper (60%) and molybdenum (95%) supply (John and Taylor 2016), as well as significant portions of gold and silver. They occur along the margins of ocean-continent subduction zones (Sillitoe 2010, Richards 2003, Sun et al. 2015), as seen around the modern-day Pacific Ring of Fire. The hydrous oceanic basalts from the subducting slab generate oxidised fluid-rich magmas that feed large (5-15km depth) calc-alkaline batholiths that form the stockwork for PCD's (Sillitoe 2010). Porphyry copper deposits are defined by a porphyritic texture with centimetre scale euhedral feldspar phenocrysts within a fine-grained silicic ground mass (typically glass), and a bulk silicic composition (Lee and Tang 2020). The porphyry body is large, and often capped by dome or bell-shaped protrusions called cupolas, which host the majority of ore. These cupolas are formed as the metalliferous hydrothermal fluids ride through the magmatic system and fracture the rock above, depositing ore minerals and altering the country rock (Sillitoe 2010).

Porphyry deposits are typically associated with highly oxidised magmas (Sillitoe 2010, Mungall 2002), and it is accepted that the oxygen fugacity (fO_2) is a direct control on metal scavenging. Lee and Tang (2020) mention that there is little evidence to suggest significant Cu input from the subducting slab, and that the copper being scavenged is of typical crustal values of ~27ppm (Rudnick et al. 2003). Jenner et al. (2010) and Lee and Tang (2020) both suggest a mineral sequestration of ferrous iron (Fe^{2+}) leaving residual ferric iron (Fe^{3+}), oxidising the magma and forming reduced mineral cumulates of magnetite (Jenner et al. 2010) and garnet (Lee and Tang 2020) at the base of the magma chamber. Oxidised magmas stall at shallow depths as pressure and temperature conditions decrease, causing exsolution of oxidised brines that effectively scavenge metal, migrating upwards, forming deposits as it cools (Lee and Tang 2020).

Whakaari and geological setting

Whakaari is a subaerial volcanic island located ~50km from the coast in the Bay of Plenty, New Zealand (Kilgour et al. 2021)(figure 2; figure 3). It forms the northern extent of the Taupo Volcanic Zone (TVZ), and has been New Zealand's most active volcano in modern history (Kilgour et al. 2021). The modern lava samples in this study were collected from the islands most recent eruptive period between 1976-2000, and the prehistoric lavas are from eruptive periods predating island monitoring (Cole et al. 2000, Heyworth et al. 2007). Whakaari and the TVZ are the product of the westward subduction of the Pacific plate beneath the Australian plate (figure 3); the oblique subduction of the Pacific plate is also causing an intra-arc extensional regime (figure 3), and is partially responsible for mantle upwelling and high geothermal gradients (Kilgour et al. 2021, Zellmer et al. 2020). The island has an intermittent crater lake (figure 2) fed by meteoric water and magmatic fluid discharge, boiling off during heightened eruptive activity, and recharging during rest. The crater lake is thought to be a sink for metals precipitating from the volcanic brines (Mandon 2017), which can be observed in surrounding sediment patterns (Hedenquist et al. 1993). These sediments, collected by Mandon et al. (2020), coupled with modern and prehistoric lava samples, are analysed in this study.

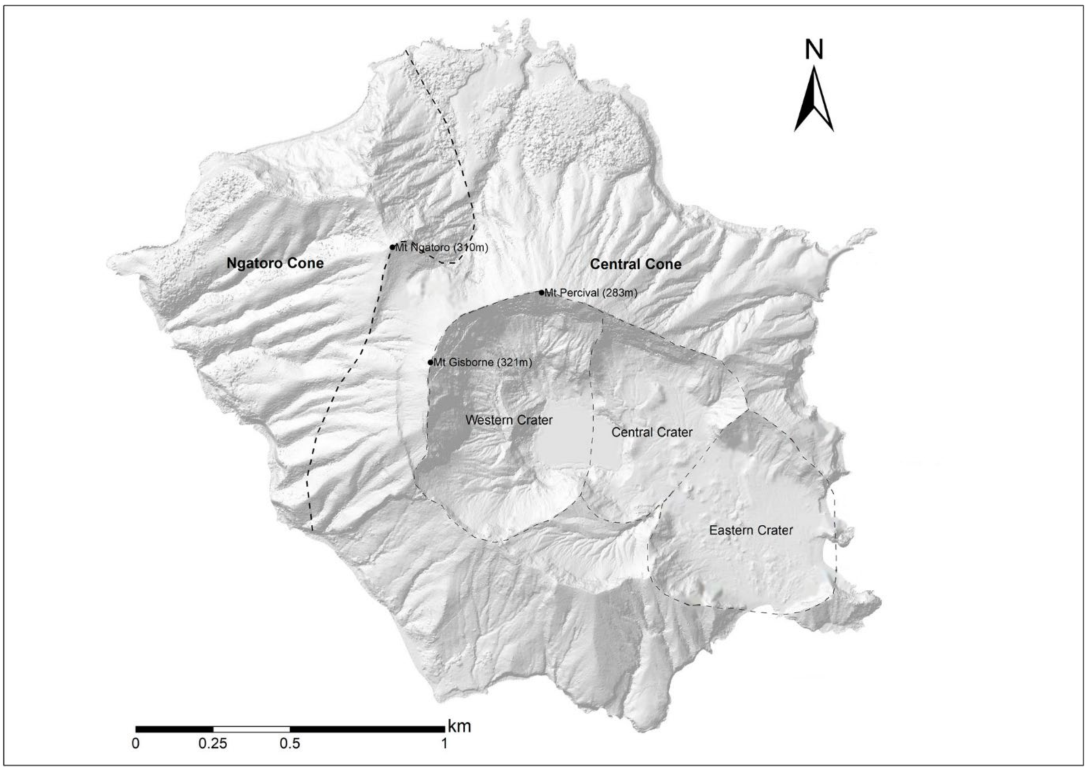

Figure 2: Digital elevation model of Whakaari. Ngatoro cone is unconformably overlain by the central cone. The western crater is the area of active vents where the current crater lake forms and acid streams discharge into the ocean from through the Eastern crater. Fumaroles are located abundantly in all three craters. Figure modified from Kilgour et al. (2021).

Whakaari is thought to be in the process of forming a porphyry copper deposit (Rapien et al. 2005, Hedenquist et al. 1993). The volcano has strongly acidic hydrothermal fluids (a strong presence of HCl and H_2SO_4) that vent at the surface and cause significant hydrothermal alteration of the host andesite, leaving behind a mineral assemblage that includes sulphates (anhydrite, alunite), silicates, and elemental sulphur in and around fumaroles. These minerals are typical of the surface expression observed at high sulphidation hydrothermal deposits (White and Hedenquist 1995, Simmons et al. 2005).

Gas monitoring during the late 1980's indicated a daily flux of ~300kg of copper from the magmatic gas plume, from a Cu/SO_2 ratio of ~$800x10^6$, and a fumarolic gas ratio of 1.6×10^6 (Le Cloarec et al. 1992). This Cu imbalance is speculated to be from a preferential partitioning of Cu into the coexisting brine, rather than vapour, and a total rate of Cu deposition of ~1-5kg/day beneath the island (Hedenquist et al. 1993). Mandon et al. (2020) further demonstrates Whakaari's ore forming potential, reporting ~4000 tonnes of Cu deposited annually.

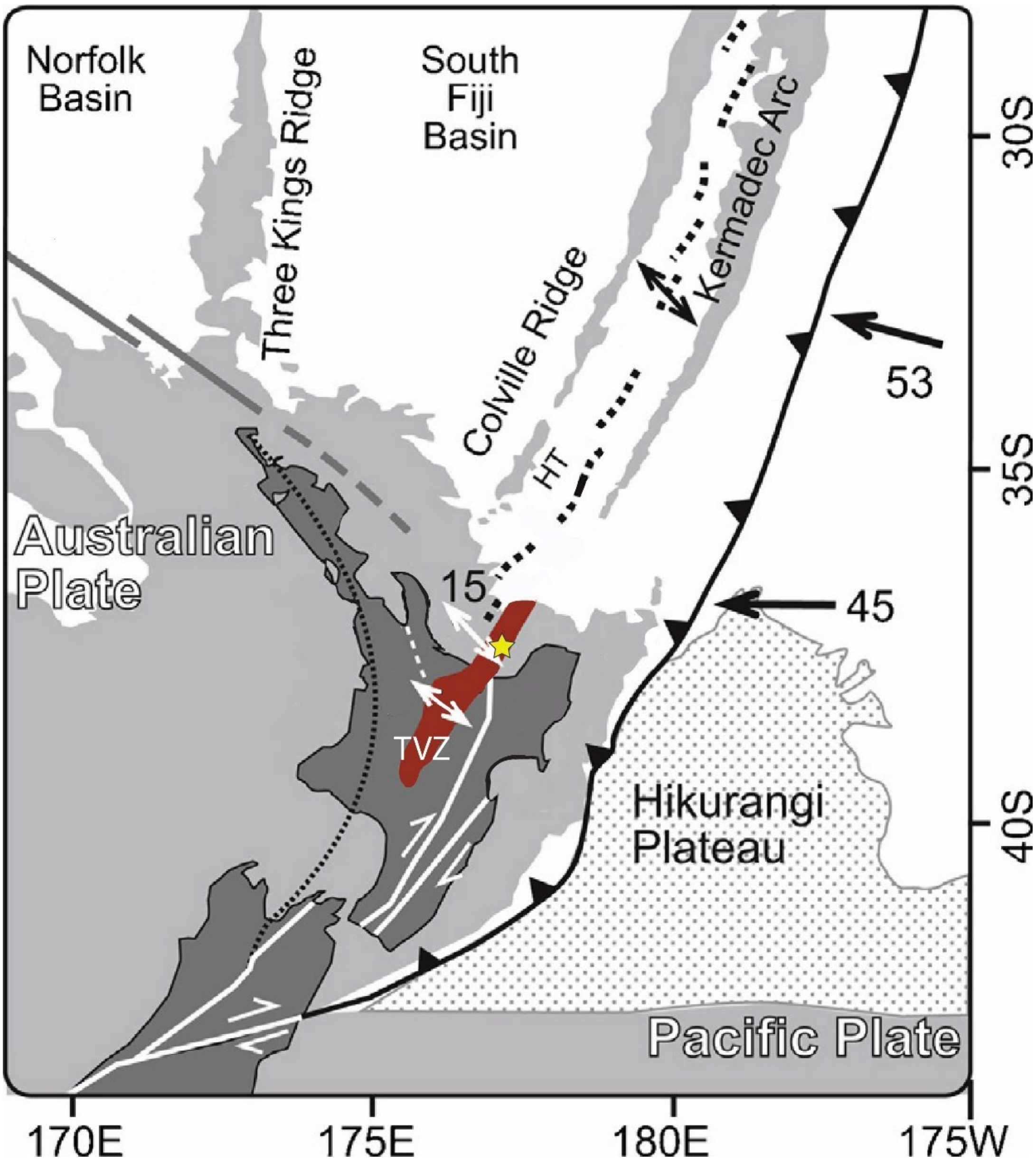

Figure 3: Tectonic setting of Whakaari, showing the westward subduction of the Pacific plate beneath the Australian plate. Taupo Volcanic Zone (TVZ) highlighted in red. Whakaari highlighted as yellow star. Extension denoted by white arrows. Modified from Wilson and Rowland (2016).

METHODS

Samples

Samples WI01, WI06 were collected on a fieldtrip to Whakaari, New Zealand on the 23rd of February, 2005 by Zarah Heyworth and Bruce Schaefer (see Heyworth et al. (2007)). Samples 880210, 891129, 911128, 920512 were collected by John Gamble and Richard Price (Gamble et al. 1990), and were used by Heyworth et al. (2007). Samples P41600, RW14, RW2, RW22, RW30, RW34, RW40, TRW17, TRW34 were collected by Jim Cole (see Cole et al. (2000), Cole and Graham (1989)). The crater lake sediments were collected by Céline L. Mandon (see Mandon et al. (2020)).

The modern lava samples are from Whakaari's most recent eruptive period, beginning in 1976, and generally show less evolved products (basaltic andesite) than the prehistoric lava of previous sequences (andesites) (Heyworth et al. 2007).

Table 1: Sample name, lab identification, Sample type, Eruption year

Sample No.	Lab	Sample Type	Rock Type	Eruption year
880210	JT1.1	Modern lava	Basaltic	1988
891129	JT1.2	Modern lava	Basaltic	1989
911128	JT1.3	Modern lava	Basaltic	1991
920512	JT1.4	Modern lava	Basaltic	1992
P41600	JT1.5	Prehistoric lava	Andesite	-
RW14	JT1.6	Prehistoric lava	Andesite	-
RW2	JT1.7	Prehistoric lava	Andesite	-
RW22	JT1.8	Prehistoric lava	Andesite	-
RW30	JT1.9	Prehistoric lava	Andesite	-
RW34	JT1.10	Prehistoric lava	Andesite	-
RW40	JT1.11	Prehistoric lava	Andesite	-
TRW17	JT1.12	Prehistoric lava	Andesite	-
TRW34	JT1.13	Modern lava	Basaltic	1977
WI01	JT1.14	Modern lava	Basaltic	2000
WI06	JT1.15	Modern lava	Basaltic	2000
JT1.10d	JT1.16	Duplicate	-	-
-	JT1.17	Blank	-	-
USGS AGV-2	JT1.18	Standard	Andesite	-
USGS BIR-1a	JT1.19	Standard	Basalt	-
Core 1-6	JT2.1	Crater lake	Sediment	-
Core 2-12	JT2.2	Crater lake	Sediment	-
Core 1-5	JT2.3	Crater lake	Sediment	-

Whole rock major element analysis

Whole rock major element analysis was provided by Wei-cheng Jiang at Macquarie University using X-ray Fluorescence at Macquarie GeoAnalytical (MQGA).

Petrography and thin sections

Thin sections provided by Wei-cheng Jiang at Macquarie University from samples used by Zarah Heyworth. The collection includes modern lavas WI06, 880210, and prehistoric lavas 891129, WI01, 911128 and 920512. Plain polarised light (PPL) and cross polarised light

(XPL) was used to identify the presence of hydrothermal alteration. Reflected light (RL) was used to detect the presence of micro-sulphides.

Solution Inductively Coupled Plasma Mass Spectrometry (Solution-ICP-MS)

All analysis involved sample digestion in HF-HNO_3 before analysis, conducted by Dr Robert Klaebe of Mawson Analytical Spectrometry Services (MASS). 0.1g of each sample, and 0.3g of RW30 was weighed for digestion. Additional RW30 was digested to have adequate Cu for analysis. Core 2-12 had remnant organics present after digestion.

Eighteen samples, two standards (USGS AGV-2, USGS BIR-1a), one duplicate (911128) and one blank were analysed using Solution ICP-MS - Agilent 8900x QQQ-ICP-MS at The University of Adelaide (Adelaide Microscopy). The two standards were analysed as unknowns, accompanied by two known standards provided by Adelaide Microscopy, and fall within 10% of reference values for most elements, except for Sm, Sc, and Rb (BIR-1a), which have errors of >30%. Other elements with >10% error have low detection or are unimportant for this study. Cu is recorded within 1.5% of reference values. Full report of standards as a percentage of reference values in appendix F.

Ion Exchange Chromatography

Digested samples underwent subsequent chemical purification and isolation of Cu via ion exchange chromatography. Samples were diluted to ~2µg Cu before being loaded into a column containing 1.5mL of AG1-x8 anionic resin (200-400 mesh). Column chromatography was run with the procedure described in table 2, based on the method by Sossi et al. (2015).

Table 2: Column chromatography expanded method

Step	Solvent	Process
Cleaning	1 cv 3M HNO3	Wash column with 3M HNO3
Cleaning	1 cv Milli-Q H2O	Wash column with milli-Q H2O
Preconditioning	1 cv 6M HCl	Wash column with 6M HCl
Sample loading	6M HCl	In 1.5ml of 6M HCl, load sample into the column
Elute matrix	6M HCl	Flush column with 7.5ml of 6M HCl in 3 x 2ml and 1x1.5ml steps to elute the matrix
Collect Cu	6M HCl	Collect Cu in Teflonware by flushing 18ml of 6M HCl in 9x2ml steps.
Drying	-	Dry down product at 110ºC

The samples were run twice through the column procedure to achieve a higher purity, removing transition metals such a Ti, Fe, and Co, which may interfere with the isotopic ratios once analysed (Hou et al. 2016).

1mL 2% HNO3 was added to the dried product. A 300µL aliquot of the 2% HNO_3 sample was pipetted into a 3mL auto sampler vial, adding 2.7mL of 2% HNO_3 to take the total volume to 3mL. This is done to dilute the sample to 200ng/mL (ppb) of Cu for analysis with MC-ICP-MS. Assuming 100% Cu yield from the columns.

Multi-Collector Inductively Coupled Plasma Mass Spectrometry (MC-ICP-MS)

Copper isotopic determination was performed using a ThermoFinnigan Neptune Multi-Collector (MC-ICP-MS) at CSIRO/The University of Adelaide Waite campus.

Standard sample bracketing was used for normalisation and a 200ppb Ga spike was used to correct for mass bias (Hou et al. 2016), with internal standard BIR-1a being run a total of four times; two initially, and two after the samples run, to measure instrument drift and to check for accuracy based on published values.

Copper isotope values are reported in standard δ-notation (per mil ‰) relative to a standard reference material (NIST976):

Equation 1:

$$\delta^{65}Cu\ ‰ = \left\{ \left(\frac{\frac{(Cu^{65})}{(Cu^{63})} sample}{\frac{(Cu^{65})}{(Cu^{63})} NIST976} \right) - 1 \right\} * 1000$$

Samples were run in sets of two, separated by a standard (NIST976). The final δ value is calculated as an average of the two runs, and a standard deviation is calculated. Voltage is also recorded.

Samples were analysed in two booking times; run one analysed JT1.1 to 11 and JT1.19 (USGS BIR-1a), and run two analysed JT1.12 to 16, JT2.1 to 3 and JT1.18 (USGS AGV-2). USGS standards were split across either run. JT1.17 (blank) was excluded from the analysis. JT1.16 (911128 duplicate) was run in the second analysis as a comparison to JT1.10 that was run in the first analysis.

Copper isotope values fall within accepted values reported in literature: **USGS-BIR-1a**: δ^{65}Cu = 0.02‰, 2*σ 0.06‰ (Moynier et al. 2017); **USGS-AGV2**: δ^{65}Cu = 0.06‰ 2*σ = 0.04‰ (Liu et al. 2014) (table 5). During the column procedure, ^{63}Cu elutes through the resin matrix faster than ^{65}Cu, due to having a smaller ionic radius. This causes up to 0.3‰ deviation from true isotopic ratios if only a 90% Cu yield is achieved (Maréchal and Albarède 2002). HCl molarity also affects the rate at which Cu is eluted through the columns, and small differences, such as 0.3M (5.7M-6M) will affect the collection of Cu, and subsequently the final δ^{65}Cu value (Hou et al. 2016). Both standards USGS-BIR-1a and USGS-AGV-2 fall within accepted reference values, and therefore it can be assumed that ~100% yield was achieved and the HCl eluent was ~6M.

Duplicates JT1.10 (δ 0.33‰) and JT1.16 (δ 0.22‰) had significant difference between measured values. This may be attributed to instrument error, as they were run in separate batches, <100% yield or heterogeneity in the sample.

Table 3: Faraday cup configuration for Cu isotope analysis on the ThermoFinnigan Neptune MC-ICP-MS.

Cup	L4	L3	L2	L1	C	H1	H2	H3	H4
Isotope	^{63}Cu	^{64}Zn	^{65}Cu	^{66}Zn	^{67}Zn	^{68}Zn	^{69}Ga	^{70}Zn	^{71}Ga

Samples were initially diluted to contain 200ng/mL (ppb); however, it was found the voltage ran too high in a test run (>10V) of the samples in the MC-ICP-MS, and the samples were subsequently diluted down to ~150ng/mL (ppb). If Cu voltage is profoundly high, then any residual matrix elements are also going to be higher, and may cause interference. Additionally, the greater the signal, the longer it takes to return to background voltage, causing needless extended run times. Extended use of excessive voltage (>20V) may also cause accelerated wear of sensors.

See appendix D.

RESULTS

Major elements

Whole rock data is presented in table 4, and are plotted against SiO_2 in figure 4. The red points represent modern lava and the black points represent prehistoric lava. The crater lake sediments were not analysed for major elements, however, as they are sediments, they are a product of their country rock and not a representation of igneous processes or magma evolution.

The modern lavas present consistently as a tight group of data points, whereas the prehistoric lavas are not tightly grouped and plot within the range of the modern samples (with the exception of MgO and Al_2O_3). FeO3 and CaO show a negative linear trend. K2O, Na_2O and MnO show positive linear trends, with one point lying outside the trend in MnO. MgO and TiO_2 present non-linear negative trends, with one non conforming point in TiO_2. Al_2O_3 presents no clear trend.

Table 4: Whole rock major element results for all samples excluding crater lake sediments.

Lab no.	Sample	SiO_2	MgO	K_2O	Na_2O	TiO_2	Al_2O_3	CaO	MnO	P_2O_5	FeO(T)	Total
JT1.1	880210	57.54	7.76	1.38	2.45	0.64	14.19	8.31	0.13	0.08	6.83	99.31
JT1.2	891129	58.04	8.21	1.39	2.39	0.63	14.24	8.45	0.14	0.08	7.00	100.57
JT1.3	911128	58.44	8.29	1.39	2.43	0.62	13.84	8.29	0.14	0.08	7.16	100.68
JT1.4	920512	58.05	8.04	1.43	2.28	0.64	13.57	8.25	0.13	0.08	6.94	99.42
JT1.5	P41600	55.26	10.33	1.12	2.18	0.62	13.41	8.58	0.14	0.07	7.34	99.06
JT1.6	RW14	57.06	4.11	1.11	2.62	0.64	17.12	7.92	0.15	0.07	7.35	98.16
JT1.7	RW2	58.95	4.41	1.37	2.67	0.58	15.98	7.53	0.14	0.07	6.91	98.61
JT1.8	RW22	55.96	6.51	0.91	2.14	0.66	16.36	8.74	0.15	0.08	7.93	99.45
JT1.9	RW30	60.70	3.65	1.44	2.72	0.58	17.02	7.70	0.13	0.08	6.32	100.34
JT1.10	RW34	57.80	3.70	1.40	2.60	0.70	16.40	7.10	0.20	0.10	7.38	97.38
JT1.11	RW40	63.24	3.52	2.29	3.16	0.75	14.72	5.47	0.10	0.11	5.63	98.99
JT1.12	TRW17	62.12	3.46	1.81	2.41	0.56	14.88	4.79	0.08	0.10	4.85	95.07
JT1.13	TRW34	58.13	8.22	1.43	2.44	0.66	13.74	8.19	0.14	0.08	7.01	100.03
JT1.14	WI01	57.80	8.09	1.40	2.37	0.66	13.70	8.13	0.14	0.08	6.98	99.33
JT1.15	WI06	56.64	7.80	1.40	2.31	0.65	13.36	8.07	0.13	0.07	6.75	97.18

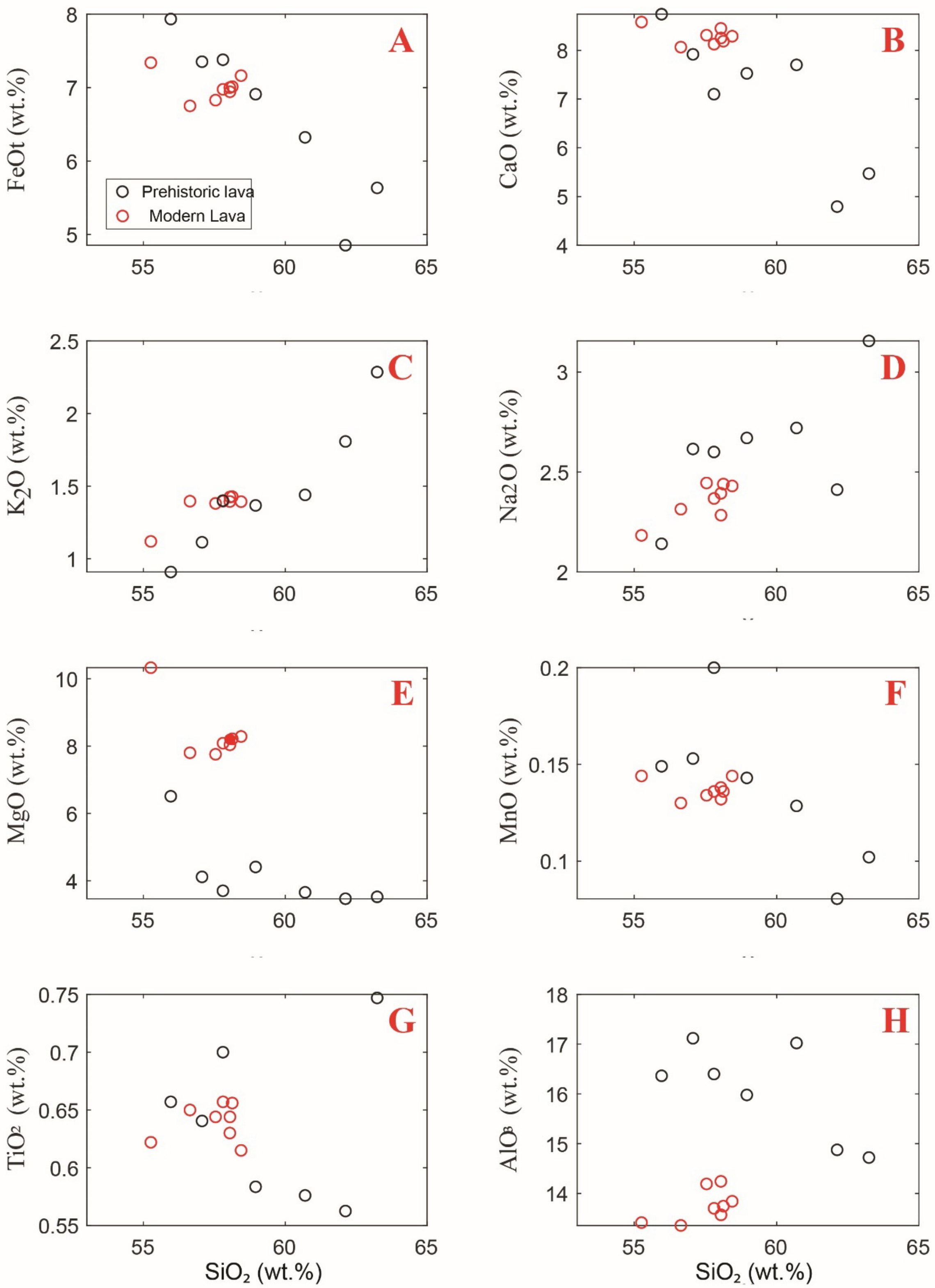

Figure 4: Harker plots of whole rock major elements for modern (red) and prehistoric (black) lavas. (A) Fe_2O_3 and SiO_2, (B) CaO and SiO_2, (C) K_2O and SiO_2, (D) Na_2 and SiO_2, (E) MgO and SiO_2, (F) MnO and SiO_2, (G) TiO_2 and SiO_2, (H) Al_2O_3 and SiO_2

Trace elements

Trace elements collected at Adelaide Microscopy through solution ICP-MS (figure 5). Trace elements are presented on a multi-element plot normalised to primitive mantle and plotted in order of compatibility. Both modern and prehistoric samples all have similar signatures, and show a typical continental arc signature. The crater lake sediments also show a signature that closely resembles a continental arc magma, with consistent depletions in mobile elements like Heavy Rare Earth Elements (HREE). JT2.2 follows a similar signature to both other sediment samples, however, exhibits an overall more depleted composition. Immobile elements like Zn and Hf have very similar enrichment to the lavas. See appendix B for full suite of trace element analysis.

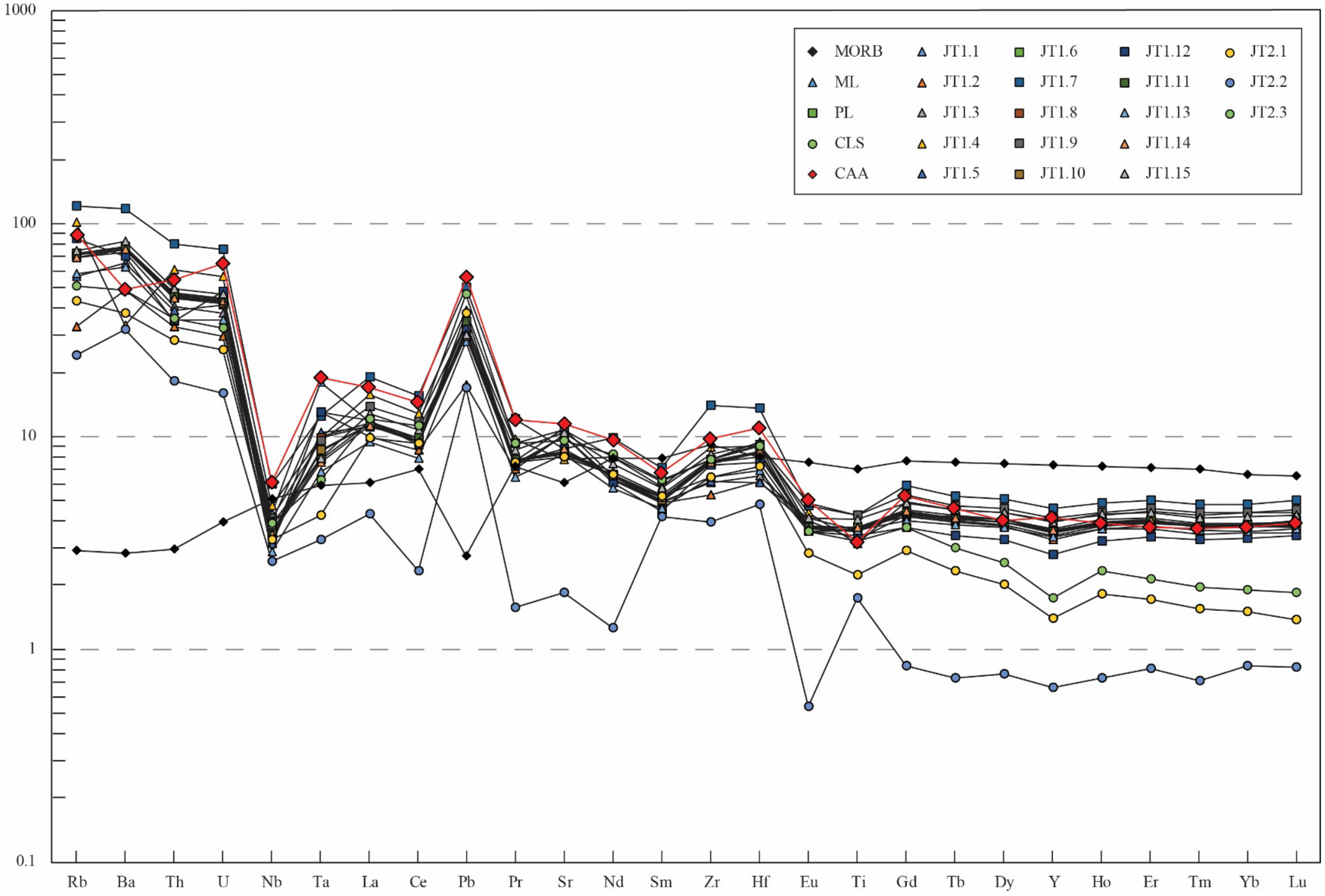

Figure 5: Trace element plot for crater lake sediments (CLS), modern lava (ML) and prehistoric lava (PL), normalised to primitive mantle (S.-S. Sun & McDonough, 1989). MORB from Gale, Dalton, Langmuir, Su, and Schilling (2013). Continental Arc Andesite (CAA) of Ruapehu from Price et al. (2012) depicted in red diamonds. Modern and prehistoric lavas closely follow a continental arc signature. Sediment signatures are more variable, but display a similar trend overall.

Petrography

Six thin sections from Whakaari were provided by Wei-Cheng Jiang of Macquarie University of the samples used by Zarah Heyworth, and comprise of two modern lavas (WI06, 820210) and four prehistoric lavas (WI01, 920512, 911128, 891129). Representative micrographs in figure 6. See appendix E for complete petrography.

The petrography revealed mineral compositions expected of andesite and basaltic andesite (i.e. presence of olivine, pyroxenes and plagioclase), and textures representative of a porphyritic rock (large phenocrysts in a fine grained or glassy groundmass).

Figure 7 shows evidence of sulphides within both the glassy groundmass (7A,B,C,D) and pyroxene (figure 7E,F). The majority of the sulphides are crystallised within the glassy groundmass of the samples.

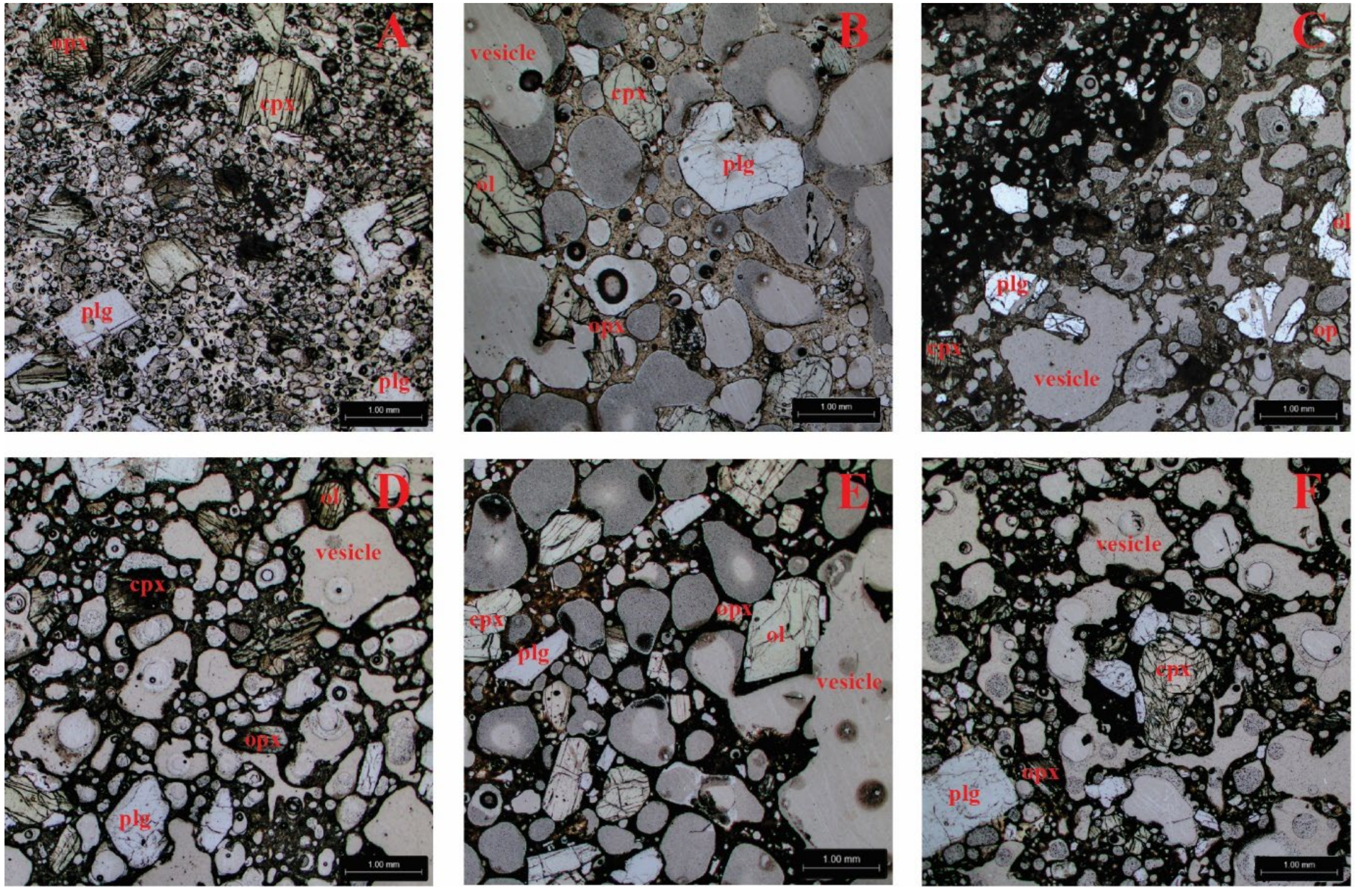

Figure 6: Micrographs of the Whakaari samples collected by Zarah Heyworth, in plain polarised (PPL), displaying representative mineralogy. All samples have a dominant porphyritic texture with plagioclase, clinopyroxene, orthopyroxene and olivine phenocrysts within a groundmass of glass and vesicles. Vesicles range from <100µm to >1mm. Plagioclase has multiple twinning and some contain oscillatory zoning. Micro-sulphides (~10µm) are present in some samples. Glomerocrysts are common. (A) Sample 880210 (B) Sample WI06 contains micro-sulphides within groundmass and orthopyroxene phenocrysts. (C) Sample 920512 has fresh and altered glass groundmass with distinct boundaries. Micro-sulphides present within the groundmass. (D) Sample 891129 Sulphides present within groundmass. (E) Sample WI01 has micro-sulphides within groundmass (F) Sample 911128 has possible minor alteration of the glass groundmass. Includes "xenocrysts" of glass within the common groundmass (appendix E, figure 4A). Micro-sulphides within groundmass.

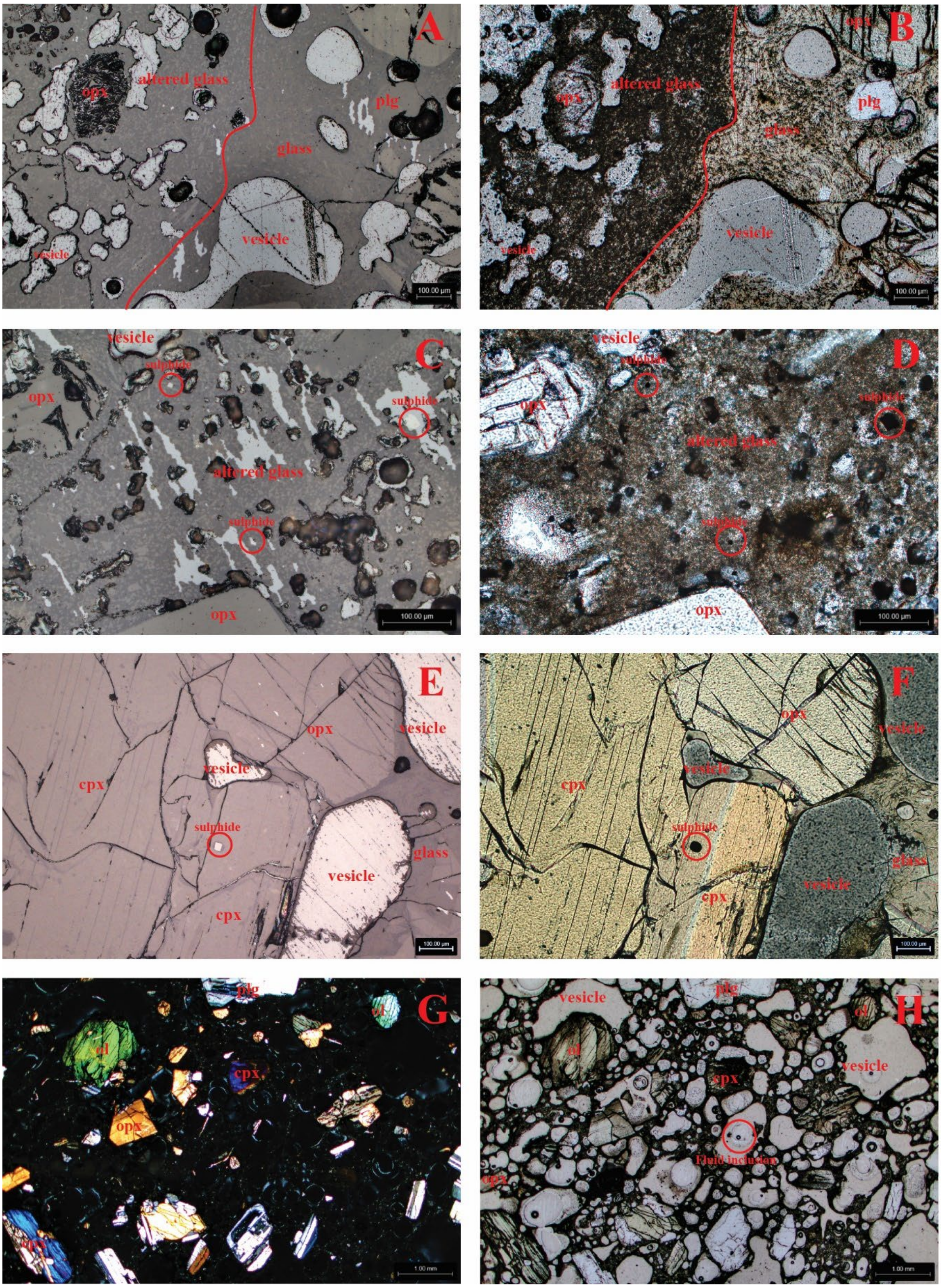

Figure 7: Micrographs of the Whakaari samples collected by Zarah Heyworth, in plain polarised (PPL), cross polarised (XPL) and reflected light (RL). (A) shows sample 911128 in reflected light, mirrored image of (B) in plain polarised light, and shows the boundary between fresh glass groundmass and dirty altered glass groundmass. (C) shows sample 920512, in reflected light, three micro-sulphides ~10um. (D) shows sample 920512 in plain polarised light, with the sulphides circled being isotropic in PPL and reflective in RL.

Copper and isotopes

Copper isotope values for the modern lava samples range between $\delta^{65}Cu$ = -0.11‰ and $\delta^{65}Cu$ = 0.45‰, copper concentrations between 49.9ppm and 87.0ppm, and sulphur concentrations between 27.6ppm and 18147.4ppm. For the prehistoric lava samples, values range between $\delta^{65}Cu$ = 0.12‰ and $\delta^{65}Cu$ = 0.59‰, copper concentrations between 26.9ppm and 89.5ppm, and sulphur concentrations between 36.2ppm and 5998.1ppm. For the crater lake sediment samples, values range between $\delta^{65}Cu$ = 0.24‰ and $\delta^{65}Cu$ = 0.40‰, copper concentrations between 29.5ppm and 37ppm, and sulphur concentrations between 115938.7ppm and 297316.9ppm (table 5).

Table 5: Copper, sulphur concentrations and copper isotope values of samples, standards and duplicate. USGS-BIR-1a and USGS-AGV2 have no reported sulphur values.

Sample	Cu (ppm)	S (ppm)	$\delta^{65}Cu$ (‰)	2*σ
JT1.1	84.8	228.2	0.16	0.008
JT1.2	49.8	1656.9	0.21	0.001
JT1.3	70.7	161.4	0.45	0.035
JT1.4	78.8	18147.4	-0.11	0.023
JT1.5	63.2	88.9	0.21	0.005
JT1.6	75.9	5998.1	0.51	0.010
JT1.7	64.5	123.6	0.59	0.011
JT1.8	89.5	273.9	0.29	0.023
JT1.9	44.2	351.3	0.091	0.031
JT1.10	80.9	140.6	0.33	0.006
JT1.11	68.4	209.9	0.43	0.036
JT1.12	26.9	36.2	0.12	0.064
JT1.13	85.7	27.6	0.37	0.003
JT1.14	87.0	274.6	0.27	0.004
JT1.15	82.2	37.2	0.32	0.019
JT2.1	29.1	120539.9	0.24	0.028
JT2.2	37.0	297316.9	0.35	0.054
JT2.3	35.2	115938.7	0.40	0.002
USGS-BIR-1a	146.4	-	0.03	0.046
USGS-AGV2	48.9	-	0.02	0.080
JT1.10 duplicate	77.8	129.1	0.22	0.049

There is very little correlation between copper and sulphur concentrations (figure 8). Similar to figure 4, there is a clustering of the modern lava samples, with the exception of two points plotting with elevated sulphur and one with less copper. The prehistoric lava samples remain variable. The crater lake sediments (CLS) have orders of magnitude more sulphur than the lavas, and relatively low Cu. Figure 8 (B) shows an inset of the same data with all samples with >1000ppm sulphur removed, as to check for trends in low sulphur samples. Despite this, there is very little correlation between S and Cu.

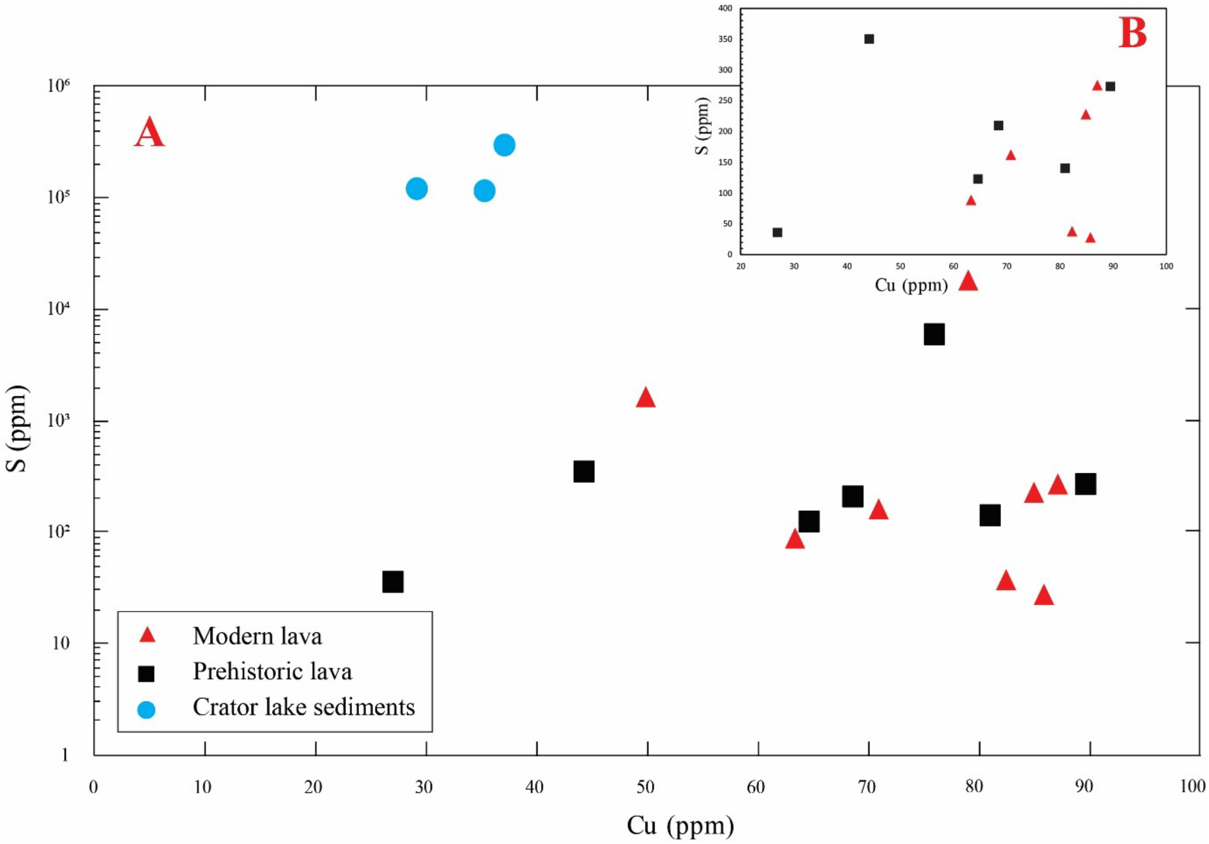

Figure 8: (A) Copper concentration of all samples plotted against sulphur concentration on log scale. (B) shows copper concentration plotted against samples with <1000ppm S on a linear scale, as crater lake sediments heavily skewed the data representation.

There is little to no correlation between δ^{65}Cu and Cu (ppm) within the Whakaari samples (figure 8). The trend of modern lava plotting closely compared to the varied spread of prehistoric lavas does not translate to the isotope values. The majority of the samples plot heavier than typical mantle values, while the data from Taranaki all plausibly fits within standard mantle values.

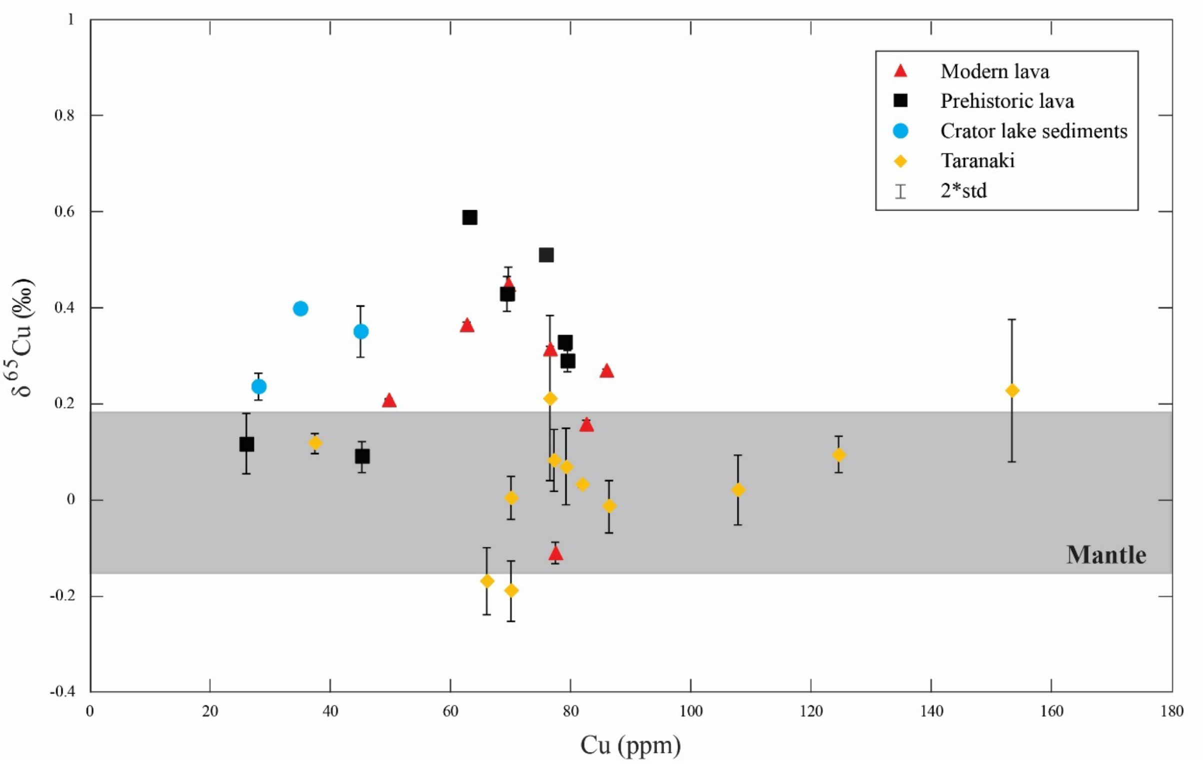

Figure 9: δ^{65}Cu values from three sources at Whakaari plotted against copper concentration. Taranaki data lies within the mantle field when errors are considered. Taranaki data from Davidson, Turner and McGee unpublished data. Typical mantle values are depicted in the grey band (Liu et al. 2015).

Figure 10a shows modern and prehistoric lavas with limited Sr variation, with no particular relation to Cu. Crater lake sediments are heavily depleted in Sr, and have less Cu than the majority of lava samples. Figure 10b shows δ^{65}Cu in respect to MgO (%) as a measure of rock revolution. There are two distinct groups, basaltic andesite (red) and andesite (grey), and two outliers.

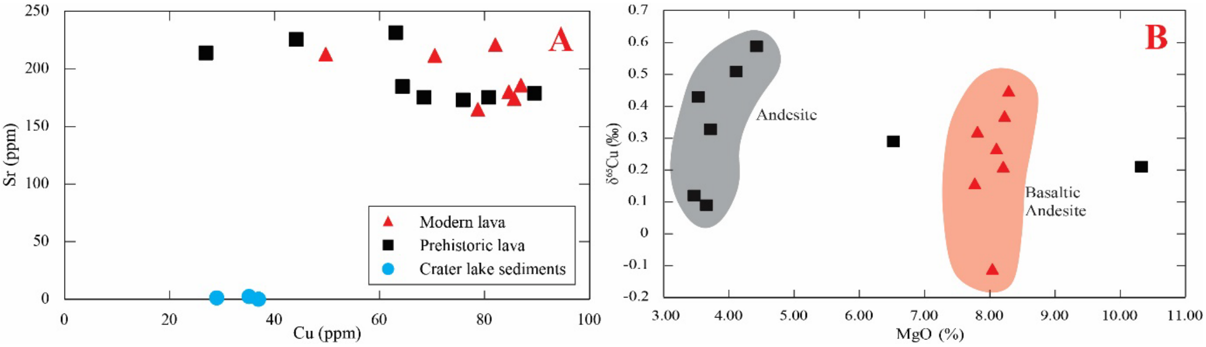

Figure 10: (A) Sr concentration plotted against Cu concentration. (B) δ65Cu values plotted against MgO (%). Two distinct compositional fields; grey representing andesite, and red, representing basaltic andesite.

DISCUSSION

Low temperature processes

Varying degrees of rock freshness is observed across the samples (figure 6,7) from petrographic analysis, and is primarily determined by cleanliness of the glass groundmass and whole rock geochemistry. Volcanic glasses, such as those found in the groundmass of extrusive igneous rocks, are chemically unstable and hydrate readily, leading to accelerated weathering and erosion (Tuffen et al. 2020). The vesicular nature of the lavas, combined with an already permeable groundmass, leads to clear pathways for hydrothermal fluids. Sample 911128 is the best example of this, showing a distinct boundary between altered and fresh glass (figure 7B), with distinct clean glass and a dirty glass, starting to break down into phyllosilicates. Other samples show evidence for hydrothermal activity to a lesser degree. Despite this, alteration does not seem advanced, such as the extent of alteration displayed within mature PCDs. The majority of samples with thin sections present as fresh extrusive igneous rocks.

Figure 10a is supplementary to the petrography, plotting Sr against Cu. Sr is mobile in fluids (Middelburg et al. 1988), and can be used as an effective proxy for weathering and alteration. Both modern and prehistoric samples show consistent Sr concentrations, however, the crater lake sediments show substantial depletion in Sr when compared to their source (lavas). The crater lake sediments are known to be interacting with acidic and oxidised fluids (Mandon 2017), and clearly demonstrates that Sr is highly mobile when interacting with fluids. When paired with sample petrography, it becomes highly unlikely that the lavas have been extensively weathered or hydrothermally altered.

Hydrothermal activity has been shown to fractionate copper in ore deposit scenarios (Maher and Larson 2007, Larson et al. 2003, Markl et al. 2006, Mathur et al. 2009). Sample 911128 has a δ^{65}Cu value of 0.45, one of the heavier isotopic signatures from the dataset (table 5). Hydrothermal alteration may impact the isotopic signature of the samples; however, most studies show that the isotopic fractionation from hydrothermal alteration is caused by the remobilisation of copper from one mineral phase to another. Sample 911128 also displays alteration affecting phenocrysts, as well as the glass (appendix B), which may indicate that minerals bearing Cu have been remobilised and light copper has been moved. If this was the case, it should be expected that the other samples have little to no variation in their isotopic signature, as 911128 is the only sample that shows alteration of the phenocrysts as well as the groundmass, which is not the case. Studies also present that the highest isotopic variations are caused by low temperature interactions (<50°C) between oxidising formation water and pre-existing sulphide mineralisation, where primary Cu(I) minerals are oxidised to secondary Cu(II) minerals (Markl et al. 2006). This type of fractionation is also documented to cause very large isotopic shifts (–16.96‰ to 9.98‰; Figure 1) (Mathur et al. 2009)**.** Figure 7C, 4D, 4E and 4F show micro sulphides (~10µm) present in some of the samples, which do not appear to be hydrothermally altered; in addition, there is also no evidence of secondary Cu (II) minerals such as malachite or covellite. Markl et al. also found that alongside isotopically heavy Cu (II) minerals, there was primary mineralisation with significantly light isotopic compositions (down to -2.92‰), proposing that the heavy ^{65}Cu was preferentially oxidised from the Cu(I) minerals to form Cu (II) minerals. If sulphides are present in all samples, this may explain why sample 920512 is isotopically light, however, there would also need to be an additional sink for heavy copper elsewhere in the system.

Markl et al. (2006) also mention the presence of isotopically light primary ore (down to -1.5 ± 0.5‰), interpreted to be formed by recycling copper from older deposits. Sample 920512 is the only isotopically negative sample in the data, and may contain sulphides formed from remobilised ore.

Whakaari is unlikely to have long-term storage of formation water, primarily due to periodic eruptions causing extreme geothermal gradients, readily observed in the vaporisation of the crater lake water (Kilgour et al. 2021). Higher temperature fluids (~400°C) are also the likely primary source of fluid in the crater lake (Mandon 2017), and are feasibly the predominant hydrothermal fluid. Consequently, it is reasonable to discount low temperature processes from being a significant contributor to copper fractionation at Whakaari.

High temperature processes

FRACTIONAL CRYSTALLISATION

The modern lava samples in this study are all basaltic andesite, and represent a less evolved body of magma beneath Whakaari when compared to the andesitic prehistoric samples (figure 4), as shown by figure 4E with modern lava having a greater MgO content, and less SiO_2. The modern samples tend to cluster closely together in composition (figure 4), likely as a consequence of being ejected in the same eruptive episode. The prehistoric lavas have a more variable composition, and their eruption ages are unknown; it is plausible that they are not all from the same eruptive period or body of magma, or a magma that has erupted, evolved, and then erupted again over a period of time. The modern lavas are less evolved than the prehistoric lavas, which may be attributed to the magma chamber recharging from a deeper, less evolved source, as Mandon (2017) suggests. This aligns with the eruptive mechanisms at Whakaari, which have been predominantly phreatic (steam-dominated) during the last eruptive cycle (Kilgour et al. 2021); a recharge of the magma chamber may cause heightened activity between the water table and the magma body, resulting in the 1975-2000 eruptive episode.

High temperature igneous processes, such as fractional crystallisation, are not commonly thought to be a primary driver of copper isotope fractionation (Moynier et al. 2017). It would be expected that if fractional crystallisation did influence copper isotopic ratios, there would be a distinct difference between the prehistoric andesite and the modern basaltic andesite Cu isotope values. This difference in isotopic signatures is not observed (figure 9, figure 10b), and instead, isotopic variation is heterogeneous throughout the evolution of the magma. Both andesite and basaltic andesite have a large spread of δ^{65}Cu values, and have significant overlap.

Rayleigh fractionation models can be helpful to show when extraction of one isotope from a phase (fluid/melt) within a closed system is occurring (figure 11). α represents the fractionation factor; 1 represents 100% of Cu remaining in fluid, and 0 represents 0% of initial copper remaining in initial fluid e.g. total incorporation into product, resulting in no fractionation. The intersect of the model and δ^{65}Cu represents the starting composition (Cu) of the rock, in this case, the highest value in the dataset, based on the assumption that the greatest Cu value represents the source rock composition. This is done as copper does not concentrate higher than the source composition when affected only by igneous processes. A typical equilibrium fractionation should show a trend where δ^{65}Cu increases exponentially with decreasing copper.

Figure 11a represents a model with a starting composition close to the expected source rock composition of Whakaari. Figure 11b represents a model created to fit the data, with arbitrary model parameters. Figure 11a shows that the isotopic composition of Whakaari does not align with what is expected from a system that only transports copper through magma evolution; likewise, the model created to fit the data uses model parameters that are unrealistic for a source composition expected at Whakaari (i.e., very high starting Cu, starting from a source that is already fractionated). This further opposes the possibility that fractional crystallisation is the cause of isotopic variation at Whakaari.

Additionally, if high temperature processes fractionated copper isotopes, we would expect to see greater variance in copper isotope signatures from Taranaki, another andesitic volcano in New Zealand's North Island. Figure 9 plots copper isotope signatures from Taranaki against the values from Whakaari, and there is a distinct difference in the spread of δ^{65}Cu values, with Taranaki showing a signature typical to mantle values reported in literature. Being an andesitic volcano, Taranaki has evidence for magma evolution through the crust, and shows very little variation in δ^{65}Cu from its likely source composition. The distinct difference between the two volcanoes indicates that there are processes occurring at Whakaari that are not affecting Taranaki, and that fractional crystallisation is not the likely cause of δ^{65}Cu variation.

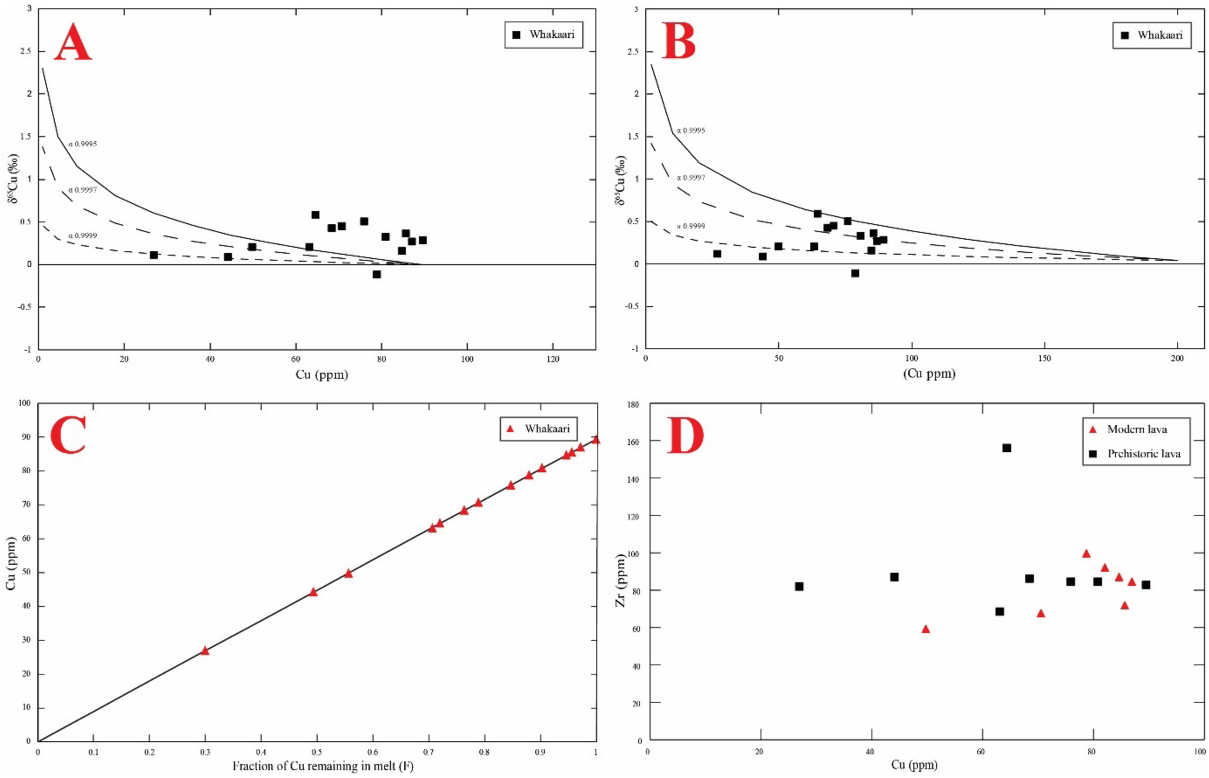

Figure 11: δ^{65}Cu values from Whakaari plotted against Cu (ppm), modelled with Rayleigh fractionation trends produced by isotopic fractionation factor α. (A) shows Rayleigh fractionation of a plausible source composition, starting at 94ppm Cu and δ^{65}Cu = 0, plotting three models with conservative fractionation factors (α) 0.9995, 0.9997 and 0.9999. (B) shows Rayleigh fractionation that fits the data from Whakaari, with arbitrary model parameters 200ppm Cu and δ^{65}Cu = 0.1, and the same conservative fractionation factors as plot A. (C) the fraction of copper remaining in melt with respect to figure 11a; sample Cu plotted against F. (D) Zr concentration plotted over Cu concentration.

Figure 11c shows the fraction of copper remaining in the melt based on the model in figure 11a; this suggests that the rocks have been formed with ~70% incorporation of copper in the melt, which indicates a high degree of crystallisation. If this were the case, figure 11d would show Zr increasing positively with Cu, and a greater range of Zr concentration when compared to Cu. This is due to Zr and Cu both being highly incompatible elements (Middelburg et al. 1988), exhibiting similar behaviours when partitioning between melt and mineral phases. However, Zr does not show a positive correlation with Cu, and little variation in Zr indicates that the lavas have been formed by a small portion of the crystallising melt, unlike figures 11a and 11c suggest. Limited positive correlation between Zr and Cu also suggests that Cu concentration is not being controlled by fractional crystallisation (figure 11a). Cu concentration is instead likely being controlled by the crystallisation of sulphides (figure 7), as even a small quantity of a Cu sulphide would increase Cu concentration. The models in figure 11 all suggest that fractional crystallisation and closed system processes are not a likely cause for isotopic variation or Cu transport.

IMMISCIBLE SULPHIDE MELT

The formation of an immiscible sulphide melt may either prevent or facilitate the formation of poprhyry copper deposits (Blundy et al. 2021, Lee and Tang 2020, Jenner et al. 2010), depending on its depth of formation. In magmas with low fO_2 (oxygen fugacity), sulphide saturation occurs deep within a magmatic system, with low total sulphur, and low metal content. The opposite occurs in systems with high fO_2, where the magmatic system has a much higher capacity to hold sulphur in melt without the onset of sulphide saturation and the formation of an immiscible sulphide melt until the magma reaches the shallow crust. It also allows for the concurrent concentration of chalcophile elements in the melt, such as copper. Large shifts in REDOX conditions have to occur to cause the precipitaiton of sulphides from a highly oxidised magma, such as those forming PCDs. Jenner et al. (2010) proposes that evolution of the magma causes magnetite to crystallise from the melt, preferentially removing Fe^{3+} from the system and leaving behind Fe^{2+}, a reduced form of Fe. The onset of magnetite crystallisation causes a decrease in fO_2, forcing sulphide saturation and formation of an immiscible sulphide melt, of which is thought to mineralise the system as it ascends and pressure and temperature drop.

Liu et al. (2023) modelled the effect that formation of an immiscible sulphide melt had on copper isotopes in a continental arc setting. The model correlates isotope signatures from lower crustal rocks and Cu-rich arc cumulates, indicating that a Rayleigh fractionation trend can be produced by the formation of sulphide melt segregation from its igneous protolith (figure 12 (trend I)). Additionally, it showed that high Cu concentration correlates with light isotope signatures from sulphide accumulation (figure 12 (trend II)).

Applying the results of this model to the data from Whakaari, it is unlikely that an immiscible sulphide melt is forming in the lower portion of the magma chamber. Deeply forming sulphide melts are also not known to be conducive to formation of a PCD, as they sequester copper in cumulates deep in the crust before it can concentrate (Sun et al. 2015); this further supports the hypothesis of Whakaari forming a porphyry copper deposit.

However, it is likely that the lavas do not represent the composition or conditions of the lower crust; figure 13 shows the possibility of magnetite fractionation occuring at Whakaari, triggering the formation of a sulphide melt much shallower in the system. At ~5.5% MgO, there is a steep decline in FeO(t) of the magma, corresponding to a steep drop in Cu at the same point. The decrease in FeO(t) is thought to reflect Fe being sequestered into magnetite, causing a REDOX shift and resulting in Cu attaching itself to SO^{2-} in a sulphide melt. This process should result in fractionation of the copper isotopes, however, it is not clearly deduced from our dataset (figure 12).

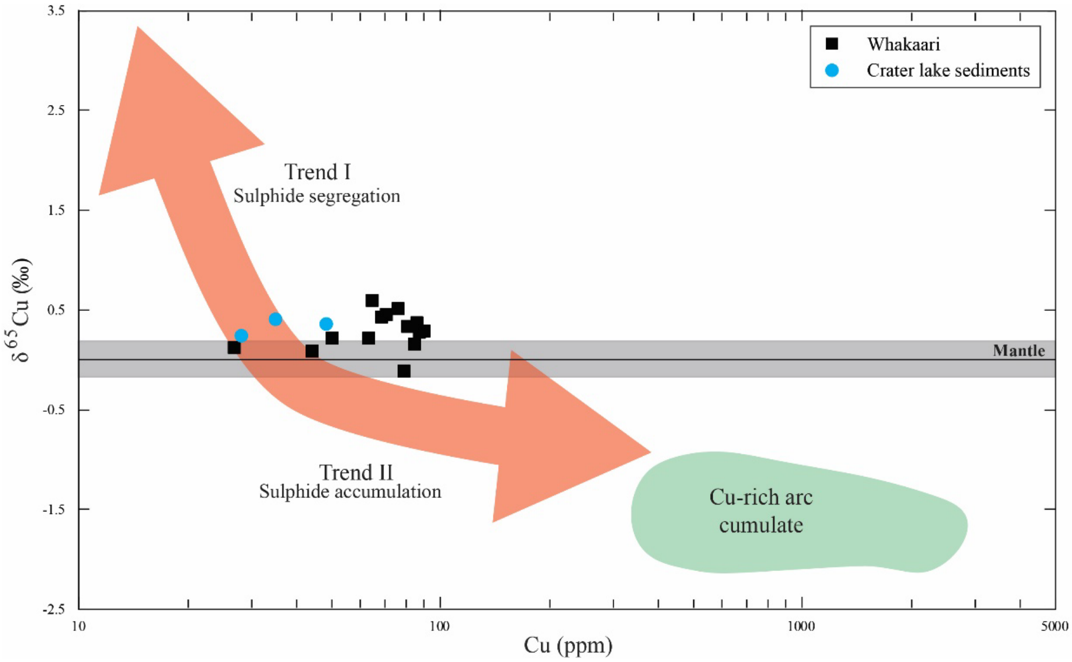

Figure 12: Depicts the fractionation trend produced by the formation of a deep immiscible sulphide melt and isotopic signatures in the subsequent formation of Cu-rich arch cumulates. Modified from Liu et al. (2023).

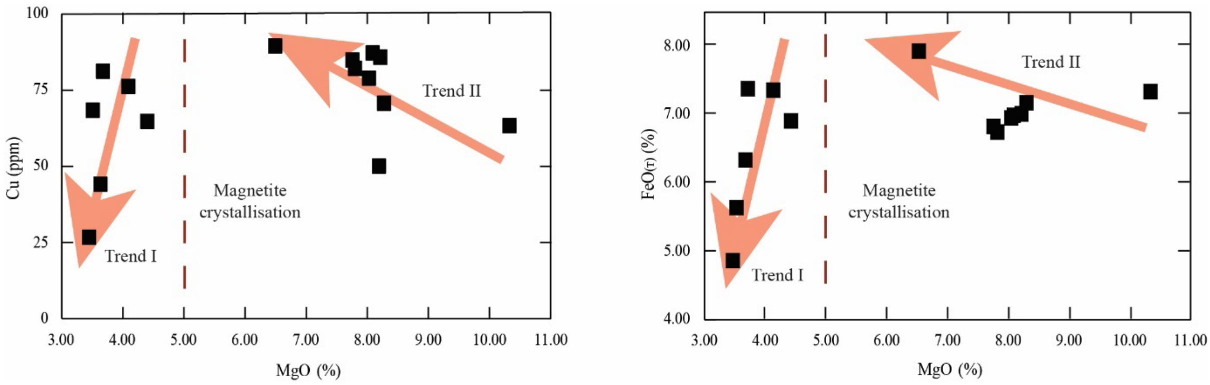

Figure 13: Cu and FeO(t) are plotted against MgO as a measure of magma evolution. Red lines indicate trends in the data, with trend II showing a steady increase of copper and iron, followed by a steep decline (trend I). Grey dotted line indicates the point of magnetite crytallisation. Based on Wang et al. (2019), Jenner et al. (2010).

Fluids

At shallow depths (~4km), decompression begins to separate the exsolved supercritical magmatic fluid into a two-phase fluid of consisting of a hypersaline brine and low-density vapour (Fournier 1999). It is these fluids that are thought to be the primary metal transport agents in the formation of PCDs, and it has been shown that they exist in fluid inclusion studies of Whakaari (Rapien et al. 2005). The brine allows enrichment of

Na, K and Fe chlorides that can concentrate between 35-70wt% NaCl, and the vapour phase carries acidic volatiles and sulphurous ligands (SO_2, H_2S, CO_2, HCl, and occasionally HF) (Giggenbach 1997), all of which facilitate metal solubility. It is the partitioning between these two phases as the system cools that is thought to be one of the primary drivers for initial isotopic fractionation of copper (Guo et al. 2020), making the brine isotopically heavy, and the vapour isotopically light.

Figure 7e and 7f show a micro-sulphide within a clinopyroxene phenocryst. The sulphide is within a fluid inclusion, indicating that metalliferous fluid was present in the magma at the time of clinopyroxene crystallisation, only precipitating sulphides as pressure and temperature lowered during magma ascent. This is interpreted that fluids are precipitating sulphides at lower temperatures, after magma crystallisation, which is what typically occurs within a porphyry copper system, forming shallow ore bodies. Sulphides are also known to precipitate from the hydrothermal fluids, as seen in the sediment core from the crater lake (figure 14). Sulphides were present in both modern and prehistoric lava samples (figure 7).

TWO PHASE FLUID

Exsolved magmatic fluid remains in a supercritical, single phase, state while at depth in the magmatic system, and splits into a two-phase fluid of high density, high salinity brine and low density, low salinity vapour as it ascends (Guo et al. 2020, Blundy et al. 2021, Mandon et al. 2020). It is the brine and vapour that are thought to be primary metal transport agents (Hedenquist and Lowenstern 1994). The petrography in figure 7 revealed the presence of sulphides primarily within the glassy matrix of the rock, apart from figure 7E/7F that shows a sulphide trapped in a fluid inclusion within a clinopyroxene. It is expected that sulphides begin to precipitate within the late stages of the magmatic system, within the top few kilometres of the crust, as the pressure reduces the saturation level of the brine and vapour. Phenocrysts begin forming within the lower bounds of the magmatic system, and can trap fluid as they crystallise. The sulphide in figure 7E/7F indicates the possibility for the presence of a copper bearing fluid in the deeper crust, while the sulphides present in the groundmass support the idea that the majority of the copper is being deposited much higher in the crust, as the glass groundmass is a consequence of instantaneous cooling from eruption. Deposition may also be controlled in the form of pulses of mineralisation (Mandon et al. 2020), caused by injection of fresh, hot magma into the existing magma chamber (Blundy et al. 2015). This is thought to cause a rapid expulsion of the brine, upward through the system, causing degassing and saturation that forces metals out of solution and into sulphides. The 1976-2000 eruptive period could be the expression of a period of fresh magma injection, as mentioned under the Fractional crystallisation discussion.

Crater lake sediments

The predominant sediment composition is likely to be an amalgamation of the many volcanic units that comprise the central cone of Whakaari, and precipitates from venting beneath the surface. Erosion of the country rock is expected to be highly physical due to the destructive nature of the island, and sediments are unlikely to be extensively weathered by meteoric water. The steep gradient of the Eastern Crater walls (figure 2), and similar elemental trends to the lava samples in the multi element plot (figure 5) supports this claim. The general trend of trace elements is very similar to the typical continental arc signature depicted in the lava samples, with the exception of mobile elements that are more depleted relative to their lava counterparts (figure 10a).

Immobile elements, such as Zn and Hf are relatively unchanged, indicating that they have not been remobilised by the crater lake waters.

The elevated sulphur in the sediments (figure 8) can likely be attributed to hydrothermal vent fluids discharging into the crater lake water, precipitating elemental sulphur and/or sulphur minerals. This is noted in Mandon et al. (2020) where the core is discoloured bright yellow due to native sulphur spherules (figure 14). Pyrite is also noted to be present within a very fine, black layer within the sediment core, however, this layer is not one of the samples analysed in this study (figure 14). It is not implausible that sulphides are also present in this sample set, just in lesser quantities. The layer of sulphides in the core is also supplementary to the idea of pulsating mineralisation, as this would have likely been caused by a large and fast influx of metalliferous fluid into the crater lake.

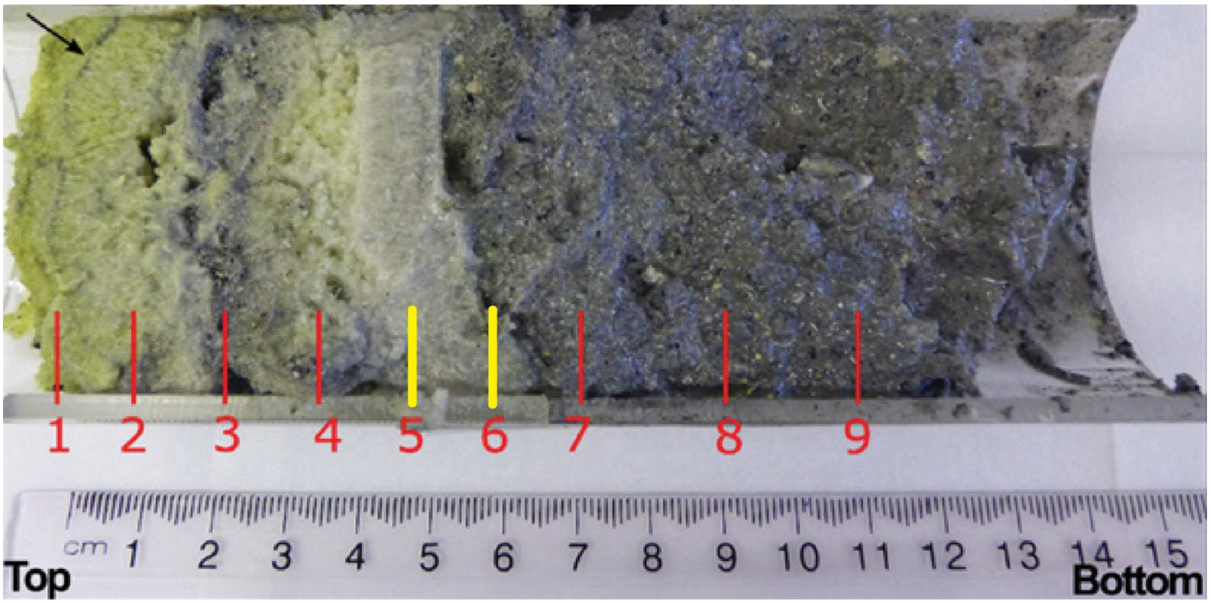

Figure 14: Image of sediments from Core 1. Increments 5 and 6, denoted in yellow, represent samples JT2.3 and JT2.1 respectively. Note a thin black layer within the yellow cap of the core (indicated by the black arrow); this is attributed to a layer of sulphur spherules containing fine grained pyrite and other sulphides. Modified from C. L. Mandon et al. (2020).

Light copper reservoir

Fractionation requires two isotopic reservoirs, one light and one heavy. Sulphides at Whakaari are the conjectured heavy reservoir of the system, and therefore need a light reservoir to be chemically balanced. The initial exsolution of fluids from the magma creates a fractionation of heavy single-phase fluid leaving residual light copper in the magma (Guo et al. 2020). Subsequent to the initial exsolution, reservoirs are not clearly defined; however, 63Cu is thought to be transported by the vapour member of the two-phase fluid (figure 15). Vapour is expressed at the surface of Whakaari as several hydrothermal endmembers, and it is likely that light copper is being sequestered in these locations: fumaroles, crater lake, and in shallow forming sulphides (Mandon et al. 2020, Kilgour et al. 2021)

Fumaroles are common on Whakaari, and are typically associated with large deposits of elemental sulphur, sulphates, and clay minerals (Kilgour et al. 2021). They are also sites of significant degassing to the atmosphere. Hedenquist et al. (1993) and Mandon (2017) found that copper from degassing fumaroles (T <500 °C) is consistently orders of magnitude less concentrated (30-80 ppb) than other samples from the island, despite mass balance calculations from the main vent (T >850 °C) indicating a much greater presence of copper. This indicates that cooling and depressurisation of the gas in shallow conduits is creating an efficient depositional environment. If the vapour is initially isotopically light, then it is reasonable to assume that the deposited sulphides are being formed from primarily 63Cu. Additionally, the copper being vented from fumaroles is likely to have an even greater negative isotopic signature, due to further kinetic fractionation leaving only small remnants of 65Cu in the vapour. Higher temperature gases, such as those from the main vent, are also likely to be isotopically light, although to a lesser extent, due to the higher temperatures retaining more copper in solution. Any copper remaining in the vapour as it degases is lost from the system to the atmosphere. Mandon et al. (2020) also found that in lower temperature environments (<500 °C) like fumaroles, sulphur is effective at sequestering transition metals into its many different forms within the hydrothermal system (e.g., elemental sulphur and sulphates).

It is unlikely that 63Cu has a single reservoir among these hydrothermal endmembers, and it is reasonable to determine that a combination of these factors would likely be the terminus for light copper at Whakaari.

Implications for the genesis of porphyry copper deposits

Whakaari is an embryonic porphyry system (Rapien et al. 2005, Hedenquist et al. 1993) forming in an environment unlike any other (Sillitoe 2010, Lee and Tang 2020). The fractionation of copper isotopes from interactions with magmatic volatiles and phase changes indicates that metals are being mobilised, transported, and concentrated without having thick, overlying crust that is commonly documented as being a primary driver of PCD formation. Furthermore, this study has recorded the transport of metals via fluid interactions that would otherwise be long lost in a mature PCD, due to destructive nature of volcanoes and the large-scale alteration characteristic of PCDs. Supergene mineralisation is a direct adversary for studying the early stages of PCD formation, as it is caused by low temperature, oxidised, hydrothermal remobilisation of metals, and overprints any isotopic fractionation caused by transport and depositional processes. Additionally, Japan has no known mature porphyry copper deposits, despite being in a tectonic setting conducive of PCD formation. Implications of metalliferous brines in embryonic systems such as Whakaari may lead to a different perspective on

PCD exploration, allowing for juvenile systems that may be present in Japan (Arribas and Mizuta 2018) to be mined with ISR techniques (Blundy et al. 2021).

CONCLUSIONS

Whakaari provides a unique opportunity to study the genesis of porphyry copper deposits, allowing for research into important embryonic processes that are otherwise lost with maturity. Petrography, whole rock major and trace element analysis and copper isotope analysis supports the following conclusions:

1. Copper fractionation is unlikely to be caused by high temperature igneous processes such as fractional crystallisation or sulphide segregation, evidenced by minimal correlation between rock evolution and copper fractionation. Similarly, there is little evidence the samples have been affected by low temperature oxidising fluids.
2. Isotopically heavy brine is a likely candidate for primary metal transport, supported by the deposition of sulphides in the glassy groundmass of lava and phenocryst fluid inclusions. Fast eruptive bursts are a feasible source of rapid depressurization and cooling, causing brines to precipitate sulphides. Magnetite crystallisation is a plausible trigger for sulphide saturation, leading to Cu deposition in the shallow crust.
3. The primary reservoir for ^{63}Cu is largely unresolved, however, light δ^{65}Cu signatures may be caused by reworking of older sulphide minerals, or deposited from isotopically light vapour. Large quantities of ^{63}Cu are plausibly being sequestered in the original magma post single-phase fluid exsolution. Small quantities of ^{63}Cu are also likely being lost to the atmosphere during shallow degassing at fumaroles.

4. There is evidence for metal transport and concentration by magma derived fluids in an embryonic porphyry copper deposit. The record of these processes is not preserved in mature PCDs due to large scale volcanic destruction, hydrothermal alteration and isotopic overprinting.

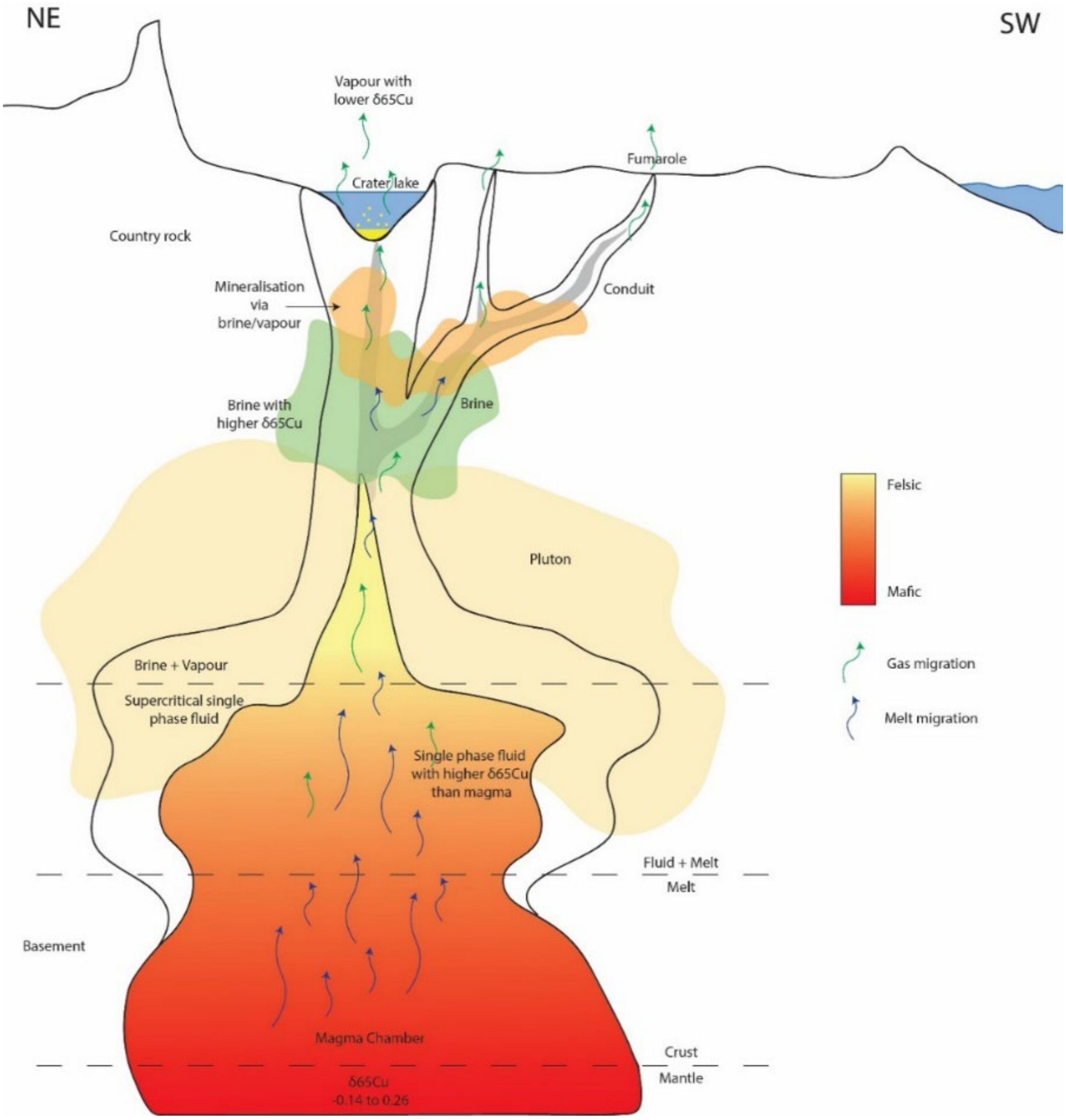

Figure 15: Cartoon model of metal transport and isotopic fractionation at Whakaari. Inspired by models from Blundy et al. (2021) Mandon et al. (2020) and Guo et al. (2020), with additional data from this study.

Future work

Analysing additional endmembers of Whakaari's hydrothermal system would provide greater insight into the total copper isotope balance and locate the ^{63}Cu reservoir. Samples from the crater lake water, crater lake scum, fumarolic native sulphur, and fumarolic gases would provide sufficient coverage across the system. Additionally, direct analysis of sulphides from the sediment core would determine with greater certainty that ^{65}Cu is preferentially forming into sulphides, or if the source of heavy ^{65}Cu is elsewhere. Iron, zinc and tin isotopes exhibit similar behaviour when interacting with REDOX changes and volatiles, and would provide complimentary data to the Cu isotopes (Creech et al. 2017, Moynier et al. 2017).

Combining samples from the surface of the island with samples from deeper in the magmatic system, such as mafic xenoliths from bombs, or a fluid inclusion study to identify trapped brine or vapour, would further the understanding of the transport system from bottom to top. Xenoliths would provide a compositional and isotopic anchor for modelling; fluid inclusions would determine the concentration of sulphur and salts present, both providing transport for copper.

ACKNOWLEDGMENTS

I would like to thank my supervisor Lucy McGee for her continuous support and guidance throughout the whole year. To Simon Turner and Wei-cheng Jiang for their help and support with samples, information, and ideas. Thanks to John Foden for his help with understanding concepts and proof reading. I am incredibly grateful to MinEx CRC and the Geological Society of Australia through the Playford Trust for their financial support. To Robert Klaebe and Simon Heinrich for their endless help and patience in the clean laboratory. Thanks to Claire Wright at the CSIRO Waite campus for help with the Neptune MC-ICP-MS. Adelaide Microscopy and Sarah Gilbert, for her help with solution ICP-MS analysis.

REFERENCES

ARRIBAS A. & MIZUTA T. 2018 Potential for porphyry copper deposits in Northern Tōhoku (or the exploration potential for base and precious metal deposits in Japan 2020), *Resource Geology,* vol. 68, no. 2, pp. 144-163.

BLUNDY J*., et al.* 2021 The economic potential of metalliferous sub-volcanic brines, *Royal Society Open Science,* vol. 8, no. 6, p. 202192.

BLUNDY J*., et al.* 2015 Generation of porphyry copper deposits by gas–brine reaction in volcanic arcs, *Nature Geoscience,* vol. 8, no. 3, pp. 235-240.

COLE J. & GRAHAM I. 1989 Petrology of strombolian and phreatomagmatic ejecta from the 1976-82 White Island eruption sequence, *NZ Geol. Surv. Bull,* vol. 103, pp. 61-68.

COLE J., THORDARSON T. & BURT R. 2000 Magma origin and evolution of White Island (Whakaari) volcano, Bay of plenty, New Zealand, *Journal of Petrology,* vol. 41, no. 6, pp. 867-895.

CREECH J., MOYNIER F. & BADULLOVICH N. 2017 Tin stable isotope analysis of geological materials by double-spike MC-ICPMS, *Chemical Geology,* vol. 457, pp. 61-67.

DOEBRICH J. 2009 Copper - A metal for the ages. In SURVEY U. S. G. ed. USGS. United States Geological Survey.

FOURNIER R. O. 1999 Hydrothermal processes related to movement of fluid from plastic into brittle rock in the magmatic-epithermal environment, *Economic Geology,* vol. 94, no. 8, pp. 1193-1211.

GAMBLE J. A*., et al.* 1990 The petrology, phase relations and tectonic setting of basalts from the Taupo Volcanic Zone, New Zealand and the Kermadec Island Arc-Havre Trough, SW Pacific, *Journal of Volcanology and Geothermal Research,* vol. 43, no. 1-4, pp. 253-270.

GIGGENBACH W. 1997 The origin and evolution of fluids in magmatic-hydrothermal systems, *Geochemistry of hydrothermal ore deposits*.

GUO H*., et al.* 2020 Experiments on Cu-isotope fractionation between chlorine-bearing fluid and silicate magma: implications for fluid exsolution and porphyry Cu deposits, *National Science Review,* vol. 7, no. 8, pp. 1319-1330.

HEDENQUIST J. W. & LOWENSTERN J. B. 1994 The role of magmas in the formation of hydrothermal ore deposits, *Nature,* vol. 370, no. 6490, pp. 519-527.

HEDENQUIST J. W*., et al.* 1993 White Island, New Zealand, volcanic-hydrothermal system represents the geochemical environment of high-sulfidation Cu and Au ore deposition, *Geology,* vol. 21, no. 8, pp. 731-734.

HEYWORTH Z*., et al.* 2007 238U–230Th–226Ra–210Pb constraints on the genesis of high-Mg andesites at White Island, New Zealand, *Chemical Geology,* vol. 243, no. 1-2, pp. 105-121.

HOU Q*., et al.* 2016 Use of Ga for mass bias correction for the accurate determination of copper isotope ratio in the NIST SRM 3114 Cu standard and geological samples by MC-ICPMS, *Journal of Analytical Atomic Spectrometry,* vol. 31, no. 1, pp. 280-287.

HSU Y.-J*., et al.* 2017 Copper partitioning between silicate melts and amphibole: Experimental insight into magma evolution leading to porphyry copper ore formation, *Chemical Geology,* vol. 448, pp. 151-163.

JENNER F. E., *et al.* 2010 The magnetite crisis in the evolution of arc-related magmas and the initial concentration of Au, Ag and Cu, *Journal of Petrology,* vol. 51, no. 12, pp. 2445-2464.

JOHN D. A. & TAYLOR R. D. 2016 By-products of porphyry copper and molybdenum deposits.

KENDALL C. & MCDONNELL J. J. 1998 Isotope tracers in catchment hydrology. Elsevier.

KILGOUR G., *et al.* 2021 Whakaari/White Island: a review of New Zealand's most active volcano, *New Zealand Journal of Geology and Geophysics,* vol. 64, no. 2-3, pp. 273-295.

LARSON P. B., *et al.* 2003 Copper isotope ratios in magmatic and hydrothermal ore-forming environments, *Chemical Geology,* vol. 201, no. 3-4, pp. 337-350.

LE CLOAREC M., *et al.* 1992 Radioactive isotopes and trace elements in gaseous emissions from White Island, New Zealand, *Earth and planetary science letters,* vol. 108, no. 1-3, pp. 19-28.

LEE C.-T. A. & TANG M. 2020 How to make porphyry copper deposits, *Earth and Planetary Science Letters,* vol. 529, p. 115868.

LIU S.-A., *et al.* 2015 Copper isotopic composition of the silicate Earth, *Earth and Planetary Science Letters,* vol. 427, pp. 95-103.

LIU S.-A., *et al.* 2014 High-precision copper and iron isotope analysis of igneous rock standards by MC-ICP-MS, *Journal of Analytical Atomic Spectrometry,* vol. 29, no. 1, pp. 122-133.

LIU S.-A., *et al.* 2023 Copper isotope evidence for sulfide fractionation and lower crustal foundering in making continental crust, *Science Advances,* vol. 9, no. 36, p. eadg6995.

MAHER K. C. & LARSON P. B. 2007 Variation in copper isotope ratios and controls on fractionation in hypogene skarn mineralization at Coroccohuayco and Tintaya, Peru, *economic geology,* vol. 102, no. 2, pp. 225-237.

MANDON C. 2017 Volatile transport of metals in the andesitic magmatic-hydrothermal system of White Island.

MANDON C. L., SEWARD T. M. & CHRISTENSON B. W. 2020 Volatile transport of metals and the Cu budget of the active White Island magmatic-hydrothermal system, New Zealand, *Journal of Volcanology and Geothermal Research,* vol. 398, p. 106905.

MARÉCHAL C. & ALBARÈDE F. 2002 Ion-exchange fractionation of copper and zinc isotopes, *Geochimica et Cosmochimica Acta,* vol. 66, no. 9, pp. 1499-1509.

MARKL G., LAHAYE Y. & SCHWINN G. 2006 Copper isotopes as monitors of redox processes in hydrothermal mineralization, *Geochimica et Cosmochimica Acta,* vol. 70, no. 16, pp. 4215-4228.

MATHUR R., *et al.* 2009 Exploration potential of Cu isotope fractionation in porphyry copper deposits, *Journal of Geochemical exploration,* vol. 102, no. 1, pp. 1-6.

MEIJA J., *et al.* 2016 Isotopic compositions of the elements 2013 (IUPAC Technical Report), *Pure and Applied Chemistry,* vol. 88, no. 3, pp. 293-306.

MIDDELBURG J. J., VAN DER WEIJDEN C. H. & WOITTIEZ J. R. 1988 Chemical processes affecting the mobility of major, minor and trace elements during weathering of granitic rocks, *Chemical geology,* vol. 68, no. 3-4, pp. 253-273.

MOYNIER F., *et al.* 2017 The isotope geochemistry of zinc and copper, *Reviews in Mineralogy and Geochemistry,* vol. 82, no. 1, pp. 543-600.

MUNGALL J. E. 2002 Roasting the mantle: Slab melting and the genesis of major Au and Au-rich Cu deposits, *Geology,* vol. 30, no. 10, pp. 915-918.

PRICE R. C.*, et al.* 2012 The anatomy of an andesite volcano: a time–stratigraphic study of andesite petrogenesis and crustal evolution at Ruapehu Volcano, New Zealand, *Journal of Petrology,* vol. 53, no. 10, pp. 2139-2189.

RAPIEN M.*, et al.* 2005 Melt inclusion study of the embryonic porphyry copper system at White Island, New Zealand.

RICHARDS J. 2003 Tectono-magmatic precursors for porphyry Cu-(Mo-Au) deposit formation, *Economic geology,* vol. 98, no. 8, pp. 1515-1533.

RUDNICK R.*, et al.* 2003 Composition of the continental crust, *The crust,* vol. 3, pp. 1-64.

SCHIPPER B. W.*, et al.* 2018 Estimating global copper demand until 2100 with regression and stock dynamics, *Resources, Conservation and Recycling,* vol. 132, pp. 28-36.

SEEDORFF E.*, et al.* 2005 Porphyry deposits: Characteristics and origin of hypogene features.

SILLITOE R. H. 2010 Porphyry copper systems, *Economic geology,* vol. 105, no. 1, pp. 3-41.

SIMMONS S. F.*, et al.* 2005 Geological Characteristics of Epithermal Precious and Base Metal Deposits. One Hundredth Anniversary Volume. pp. 0. Society of Economic Geologists.

SOSSI P. A.*, et al.* 2015 Combined separation of Cu, Fe and Zn from rock matrices and improved analytical protocols for stable isotope determination, *Geostandards and Geoanalytical Research,* vol. 39, no. 2, pp. 129-149.

SUN W.*, et al.* 2015 Porphyry deposits and oxidized magmas, *Ore Geology Reviews,* vol. 65, pp. 97-131.

TUFFEN H.*, et al.* 2020 Obsidian. Encyclopedia of Geology: Volume 1-6, Second Edition. pp. 196-208.

VANCE D.*, et al.* 2008 The copper isotope geochemistry of rivers and the oceans, *Earth and Planetary Science Letters,* vol. 274, no. 1-2, pp. 204-213.

WANG Z.*, et al.* 2019 Evolution of copper isotopes in arc systems: Insights from lavas and molten sulfur in Niuatahi volcano, Tonga rear arc, *Geochimica et Cosmochimica Acta,* vol. 250, pp. 18-33.

WHITE N. C. & HEDENQUIST J. W. 1995 Epithermal Gold Deposits: STYLES, CHARACTERISTICS AND EXPLORATION, *SEG Discovery*, no. 23, pp. 1-13.

WILSON C. J. & ROWLAND J. V. 2016 The volcanic, magmatic and tectonic setting of the Taupo Volcanic Zone, New Zealand, reviewed from a geothermal perspective, *Geothermics,* vol. 59, pp. 168-187.

ZELLMER G. F.*, et al.* 2020 Genesis of recent mafic magmatism in the Taupo Volcanic Zone, New Zealand: insights into the birth and death of very large volume rhyolitic systems?, *Journal of Petrology,* vol. 61, no. 2, p. egaa027.

APPENDIX A: GRAPHS

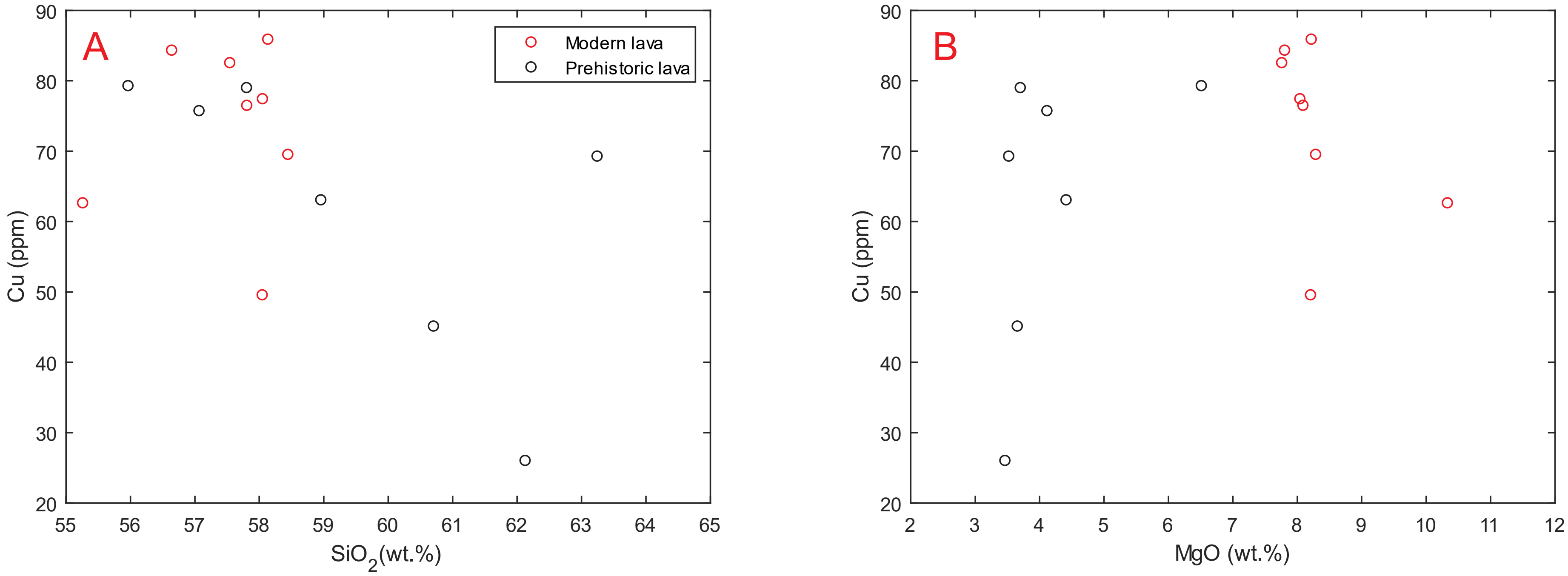

Figure I: (A) Cu and SiO_2, and (B) Cu and MgO.

APPENDIX B: SOLUTION ICP-MS RAW DATA

Solution ICP-MS trace element raw data in ppb.
Run 1:

Sample	7 -> 7 Li	9 -> 9 Be	11 -> 11 B	31 -> 47 P	32 -> 48 S	34 -> 50 S	45 -> 61 Sc
JT1.1	19.54	0.65	18.98	342.68	228.19	255.55	24.06
JT1.2	6.01	0.58	12.66	332.32	1656.89	2033.74	24.67
JT1.3	13.73	0.76	16.72	283.91	161.38	192.69	22.13
JT1.4	7.87	1.26	27.34	394.74	18147.35	21865.76	18.02
JT1.5	20.15	0.75	22.51	297.64	88.93	106.56	22.34
JT1.6	18.04	0.61	21.27	315.72	5998.09	7366.71	25.60
JT1.7	29.28	0.98	31.77	455.74	123.63	175.03	17.14
JT1.8	22.49	0.70	24.59	342.26	273.91	372.31	26.17
JT1.9	19.14	0.81	20.97	395.61	351.33	467.43	19.94
JT1.10	20.19	0.65	19.65	313.05	140.57	191.38	23.58
JT1.11	20.00	0.58	20.54	303.18	209.86	251.47	22.05
JT1.12	16.94	0.90	13.84	299.31	36.24	73.89	14.15
JT1.13	18.00	0.67	16.60	272.91	27.63	58.11	23.14
JT1.14	23.46	0.74	25.21	334.26	274.59	337.27	25.10
JT1.15	21.56	0.63	20.36	320.61	37.21	56.89	22.79
JT1.16	21.16	0.64	17.74	297.64	129.06	180.74	21.30
JT1.17	<0.090	<0.026	<0.575	<2.243	<21.128	<41.160	<0.006
JT1.18	13.06	2.52	5.61	1705.79	<21.128	<41.160	8.07
JT1.19	4.35	0.11	0.64	83.69	<21.128	<41.160	28.68

Run 2:

Sample	7 -> 7 Li	23 -> 23 Na	24 -> 24 Mg	27 -> 27 Al	28 -> 44 Si	29 -> 45 Si	31 -> 31 P
JT2.1	5.65	4134.23	3010.17	23969.15	<18.182	<38.467	221.35
JT2.2	3.62	2360.09	1648.89	7698.03	<18.182	<38.467	<204.154
JT2.3	4.66	3434.57	2401.42	20765.45	<18.182	<38.467	<204.154

Sample	47 -> 79 Ti	49 -> 81 Ti	51 -> 83 V	52 -> 68 Cr	55 -> 71 Mn	59 -> 59 Co	59 -> 75 Co
JT1.1	4904.38	4985.42	245.81	424.94	1166.90	37.98	35.67
JT1.2	4901.29	4879.01	281.63	148.33	1241.64	34.24	32.05
JT1.3	4355.45	4323.58	235.89	47.39	1254.29	31.04	28.98
JT1.4	4300.22	4142.37	144.61	152.51	697.18	41.65	38.75
JT1.5	4977.38	4743.19	254.91	31.61	1290.36	37.89	35.52
JT1.6	4840.25	4630.26	238.02	397.93	1129.58	35.15	32.59
JT1.7	5922.56	5652.33	217.70	111.19	894.37	27.56	25.81
JT1.8	5381.67	5242.72	268.64	496.95	1321.41	38.35	35.72
JT1.9	5495.57	5416.76	273.02	46.29	1265.19	37.92	35.16
JT1.10	4878.47	4889.05	248.41	400.83	1218.70	34.70	32.32
JT1.11	4693.59	4794.44	239.35	407.36	1171.13	33.88	31.74
JT1.12	4492.99	4570.64	227.80	16.82	1154.40	25.14	23.64
JT1.13	4633.15	4720.38	247.23	579.38	1273.30	41.76	39.21
JT1.14	5327.37	5542.01	283.81	482.98	1375.15	39.94	37.36
JT1.15	4980.13	5170.42	264.96	554.45	1221.99	37.42	34.98
JT1.16	4761.61	5023.28	254.41	418.61	1278.52	35.97	33.74
JT1.17	0.55	0.53	0.03	<0.513	0.05	<0.017	<0.034
JT1.18	7555.28	7975.78	113.89	17.25	891.46	16.36	15.41
JT1.19	8928.60	9183.31	475.75	543.26	1888.71	68.11	63.52

Run 2:

Sample	32 -> 48 S	39 -> 39 K	43 -> 59 Ca	44 -> 60 Ca	45 -> 61 Sc	47 -> 79 Ti	49 -> 81 Ti
JT2.1	136920.10	7575.34	72678.83	76549.09	6.02	4572.02	4566.28
JT2.2	298212.32	2280.65	2630.04	3390.36	2.35	2825.18	2760.39
JT2.3	119814.85	6642.90	63023.28	67262.35	5.04	4061.34	4033.99

Sample	60 -> 60 Ni	60 -> 76 Ni	65 -> 65 Cu	66 -> 66 Zn	69 -> 69 Ga	71 -> 71 Ga	71 -> 71 Ga
JT1.1	120.90	121.45	84.77	64.32	50.90	13.97	14.11
JT1.2	44.92	43.67	49.84	65.66	38.79	15.11	15.28
JT1.3	19.47	19.24	70.68	70.73	49.35	15.94	15.39
JT1.4	115.22	115.15	78.83	84.14	30.47	15.58	15.33
JT1.5	18.91	18.44	63.24	75.29	48.52	16.86	16.61
JT1.6	117.01	115.74	75.88	61.68	47.26	13.45	13.23
JT1.7	43.96	43.75	64.53	60.80	70.49	15.55	15.53
JT1.8	120.10	118.39	89.53	70.58	53.45	15.43	15.42
JT1.9	19.19	19.35	44.16	76.72	50.29	16.01	16.04
JT1.10	110.89	110.01	80.87	66.11	49.69	13.78	14.00
JT1.11	118.24	117.69	68.39	78.27	48.04	13.35	13.40
JT1.12	6.07	5.60	26.86	65.18	50.14	16.71	16.59
JT1.13	196.18	193.27	85.68	65.64	42.61	13.33	13.08
JT1.14	136.63	136.24	87.01	71.27	53.55	15.18	15.35
JT1.15	129.84	130.60	82.20	63.78	50.44	14.22	14.34
JT1.16	115.59	114.27	77.78	65.74	48.60	13.68	13.71
JT1.17	<0.093	<0.165	<0.036	1.23	<0.008	<0.010	0.00
JT1.18	18.56	18.24	48.99	89.89	99.83	20.52	21.78
JT1.19	218.09	218.65	146.49	95.46	18.80	19.55	19.32

Run 2:

Sample	51 -> 83 V	52 -> 68 Cr	55 -> 71 Mn	56 -> 72 Fe	57 -> 73 Fe	59 -> 59 Co	60 -> 60 Ni
JT2.1	56.71	62.96	101.27	11117.47	12491.72	5.62	13.66
JT2.2	19.84	20.14	53.64	6675.57	7463.35	5.99	13.94
JT2.3	48.34	53.73	85.09	10392.23	11734.40	5.30	13.31

Sample	72 -> 88 Ge	73 -> 89 Ge	85 -> 85 Rb	88 -> 104 Sr	89 -> 105 Y	90 -> 122 Zr	93 -> 125 Nb
JT1.1	<0.193	<0.168	47.46	184.32	17.09	89.22	3.19
JT1.2	<0.193	<0.168	20.86	214.27	15.06	59.66	2.29
JT1.3	<0.193	<0.168	44.87	214.94	15.84	69.07	2.38
JT1.4	<0.193	<0.168	65.74	167.52	18.62	101.23	3.40
JT1.5	<0.193	<0.168	36.34	233.21	16.61	69.59	2.26
JT1.6	<0.193	<0.168	45.16	173.72	16.19	84.46	2.49
JT1.7	<0.193	<0.168	78.50	189.15	21.26	159.84	4.37
JT1.8	<0.193	<0.168	49.24	202.02	18.09	93.71	2.79
JT1.9	<0.193	<0.168	44.90	220.91	18.39	85.24	2.87
JT1.10	<0.193	<0.168	47.22	179.62	16.67	86.67	2.58
JT1.11	<0.193	<0.168	45.61	173.42	16.14	85.15	2.50
JT1.12	<0.193	<0.168	55.49	220.12	12.99	84.78	2.90
JT1.13	<0.193	<0.168	36.74	174.17	15.17	71.68	2.03
JT1.14	<0.193	<0.168	50.21	210.94	18.70	96.09	2.82
JT1.15	<0.193	<0.168	45.85	215.27	17.48	90.34	2.67
JT1.16	<0.193	<0.168	45.95	177.58	16.80	87.29	2.56
JT1.17	<0.193	<0.168	<0.024	0.02	<0.002	<0.014	<0.011
JT1.18	<0.193	<0.168	70.82	706.01	16.95	243.57	11.86
JT1.19	<0.193	<0.168	0.12	129.86	15.82	16.24	0.64

Run 2:

Sample	63 -> 63 Cu	63 -> 79 Cu	65 -> 65 Cu	66 -> 82 Zn	69 -> 69 Ga	71 -> 71 Ga	75 -> 91 As
JT2.1	38.41	1043.56	37.52	24.42	30.13	5.22	18.08
JT2.2	38.79	521.63	37.36	14.28	17.97	1.62	195.34
JT2.3	32.94	809.66	31.84	21.13	27.77	4.77	18.71

Sample	95 -> 95 Mo	95 -> 111 Mo	111 -> 111 Cd	118 -> 118 Sn	118 -> 118 Sn	118 -> 118 Sn	133 -> 133 Cs
JT1.1	0.81	0.74	0.09	0.91	0.94	0.93	2.58
JT1.2	0.54	0.53	0.09	0.67	0.69	0.66	0.65
JT1.3	0.47	<0.329	0.12	0.77	0.79	0.73	1.68
JT1.4	0.62	0.64	0.16	1.26	1.24	1.18	2.67
JT1.5	0.59	0.66	0.08	0.78	0.83	0.78	1.92
JT1.6	0.69	0.66	0.09	1.43	1.43	1.36	2.56
JT1.7	1.08	1.21	0.08	1.32	1.36	1.28	4.34
JT1.8	0.95	1.25	0.10	1.01	1.00	0.97	2.66
JT1.9	0.70	0.59	0.11	0.88	0.96	0.87	2.57
JT1.10	0.74	0.73	0.09	0.85	0.87	0.82	2.61
JT1.11	0.71	0.66	0.09	1.15	1.12	1.09	2.51
JT1.12	0.66	0.60	0.06	0.62	0.63	0.61	1.63
JT1.13	1.94	1.94	0.11	1.20	1.19	1.14	2.18
JT1.14	0.79	0.99	0.08	1.05	1.08	1.02	2.87
JT1.15	0.96	0.73	0.08	1.00	0.99	0.96	2.61
JT1.16	0.71	0.82	0.09	0.89	0.92	0.87	2.49
JT1.17	<0.011	<0.329	0.00	0.02	<0.020	0.02	<0.013
JT1.18	2.05	2.31	0.11	2.12	2.24	2.12	1.21
JT1.19	0.04	<0.329	0.10	0.84	0.87	0.84	<0.013

Run 2:

Sample	85 -> 85 Rb	88 -> 104 Sr	89 -> 105 Y	90 -> 122 Zr	93 -> 125 Nb	95 -> 95 Mo	97 -> 97 Mo
JT2.1	34.18	224.39	8.87	112.27	3.10	1.21	1.22
JT2.2	15.70	44.50	3.10	48.86	1.95	1.01	1.00
JT2.3	31.02	197.83	7.47	100.35	2.78	1.20	1.18

Sample	137 -> 153 Ba	139 -> 155 La	140 -> 156 Ce	141 -> 157 Pr	146 -> 162 Nd	147 -> 163 Sm	153 -> 169 Eu
JT1.1	559.21	8.23	17.80	2.19	9.41	2.41	0.65
JT1.2	343.25	6.90	15.36	1.96	8.46	2.16	0.64
JT1.3	520.31	8.08	17.31	2.09	8.74	2.23	0.68
JT1.4	235.72	10.91	23.05	2.73	10.99	2.60	0.75
JT1.5	463.12	7.65	17.52	2.14	8.90	2.19	0.70
JT1.6	525.15	7.79	16.90	2.12	8.95	2.31	0.63
JT1.7	842.57	13.36	28.19	3.41	13.67	3.26	0.81
JT1.8	594.24	8.70	19.06	2.36	9.90	2.47	0.70
JT1.9	528.49	9.20	20.39	2.50	10.58	2.68	0.80
JT1.10	546.87	8.00	17.25	2.16	9.10	2.29	0.62
JT1.11	537.17	7.81	17.29	2.10	8.76	2.26	0.62
JT1.12	502.85	8.40	16.69	2.07	8.48	2.04	0.62
JT1.13	434.95	6.45	13.94	1.77	7.67	2.03	0.60
JT1.14	602.38	8.80	19.09	2.38	10.02	2.58	0.70
JT1.15	559.70	8.54	18.53	2.30	9.75	2.47	0.68
JT1.16	541.59	8.05	17.30	2.13	9.09	2.32	0.62
JT1.17	0.02	<0.002	0.00	<0.002	<0.008	<0.008	<0.001
JT1.18	1159.33	36.06	64.66	7.53	28.58	5.14	1.41
JT1.19	7.49	0.69	2.10	0.41	2.67	1.25	0.60

Run 2:

Sample	107 -> 107 Ag	109 -> 109 Ag	111 -> 111 Cd	118 -> 118 Sn	118 -> 118 Sn	118 -> 118 Sn	121 -> 121 Sb
JT2.1	0.08	0.04	0.08	1.44	1.50	1.40	1.99
JT2.2	0.04	0.02	0.08	0.95	0.97	0.95	1.56
JT2.3	0.07	0.03	0.08	1.36	1.38	1.33	1.90

Sample	157 -> 173 Gd	159 -> 175 Tb	163 -> 179 Dy	165 -> 181 Ho	166 -> 182 Er	169 -> 185 Tm	172 -> 188 Yb
JT1.1	2.76	0.47	3.09	0.68	2.05	0.30	1.97
JT1.2	2.52	0.43	2.79	0.60	1.78	0.26	1.74
JT1.3	2.57	0.44	2.90	0.64	1.91	0.28	1.91
JT1.4	3.01	0.49	3.27	0.71	2.16	0.32	2.20
JT1.5	2.64	0.45	2.95	0.63	1.92	0.28	1.87
JT1.6	2.61	0.45	2.92	0.63	1.92	0.28	1.87
JT1.7	3.57	0.58	3.82	0.82	2.45	0.36	2.40
JT1.8	2.90	0.50	3.27	0.72	2.15	0.32	2.09
JT1.9	3.11	0.50	3.30	0.70	2.14	0.32	2.13
JT1.10	2.65	0.46	3.07	0.65	1.96	0.29	1.94
JT1.11	2.59	0.44	2.89	0.64	1.92	0.27	1.86
JT1.12	2.28	0.38	2.47	0.54	1.66	0.25	1.68
JT1.13	2.39	0.41	2.76	0.60	1.80	0.27	1.75
JT1.14	3.00	0.51	3.42	0.74	2.19	0.32	2.14
JT1.15	2.83	0.47	3.16	0.69	2.06	0.30	2.02
JT1.16	2.70	0.45	2.96	0.65	1.93	0.29	1.88
JT1.17	<0.005	<0.001	<0.003	<0.002	0.00	<0.002	<0.009
JT1.18	4.25	0.56	3.23	0.63	1.72	0.24	1.47
JT1.19	2.16	0.41	2.95	0.65	1.96	0.28	1.85

Run 2:

Sample	121 -> 121 Sb	125 -> 125 Te	125 -> 125 Te	133 -> 133 Cs	137 -> 153 Ba	139 -> 155 La	140 -> 156 Ce
JT2.1	2.00	3.21	3.21	3.59	436.98	8.90	21.88
JT2.2	1.62	20.97	21.05	2.18	289.79	3.08	4.38
JT2.3	1.91	2.89	2.73	3.26	413.76	8.00	19.58

Sample	175 -> 191 Lu	178 -> 178 Hf	178 -> 194 Hf	181 -> 181 Ta	181 -> 197 Ta	182 -> 182 W	205 -> 205 Tl
JT1.1	0.30	2.76	2.99	0.75	0.53	66.12	0.18
JT1.2	0.26	1.93	1.91	0.54	0.39	53.40	0.27
JT1.3	0.29	2.13	2.04	0.42	0.30	41.52	0.19
JT1.4	0.33	3.07	2.83	0.41	0.34	22.65	0.79
JT1.5	0.29	2.23	1.89	0.43	0.29	80.95	0.05
JT1.6	0.28	2.68	2.49	0.35	0.27	2.99	0.22
JT1.7	0.38	4.27	4.29	0.52	0.47	82.99	0.32
JT1.8	0.32	2.97	2.94	0.46	0.33	3.40	0.20
JT1.9	0.33	2.69	2.77	0.39	0.29	94.41	0.30
JT1.10	0.30	2.77	2.63	0.36	0.28	2.57	0.16
JT1.11	0.29	2.69	2.59	0.32	0.24	2.24	0.17
JT1.12	0.26	2.58	2.40	0.55	0.42	37.61	0.15
JT1.13	0.27	2.28	2.13	0.28	0.25	2.42	0.13
JT1.14	0.33	2.98	2.99	0.35	0.27	2.19	0.13
JT1.15	0.31	2.78	2.81	0.31	0.27	2.53	0.12
JT1.16	0.29	2.69	2.71	0.33	0.27	2.09	0.14
JT1.17	<0.003	<0.009	<0.247	0.02	<0.020	0.48	<0.004
JT1.18	0.23	4.90	5.00	0.80	0.74	1.94	0.24
JT1.19	0.27	0.70	0.71	0.25	0.17	1.72	<0.004

Run 2:

Sample	141 -> 157 Pr	146 -> 162 Nd	147 -> 163 Sm	153 -> 169 Eu	157 -> 173 Gd	159 -> 175 Tb	163 -> 179 Dy
JT2.1	2.83	11.79	2.79	0.65	2.41	0.36	2.09
JT2.2	0.46	1.80	0.46	0.10	0.50	0.09	0.57
JT2.3	2.52	10.33	2.44	0.58	2.13	0.31	1.83

Sample	206 -> 206 [Pb]	207 -> 207 [Pb]	208 -> 208 Pb	232 -> 232 Th	238 -> 238 U
JT1.1	6.64	6.39	6.49	3.94	0.92
JT1.2	3.38	3.22	3.30	2.78	0.62
JT1.3	5.84	5.57	5.73	3.51	0.81
JT1.4	7.70	7.36	7.54	5.24	1.21
JT1.5	5.96	5.76	5.85	3.33	0.88
JT1.6	6.05	5.82	5.96	3.87	0.91
JT1.7	9.88	9.48	9.75	6.94	1.61
JT1.8	6.82	6.55	6.64	4.27	0.99
JT1.9	6.25	6.09	6.17	3.90	0.92
JT1.10	6.20	6.03	6.13	4.02	0.94
JT1.11	6.43	6.36	6.41	3.90	0.91
JT1.12	6.38	6.16	6.26	3.03	1.04
JT1.13	5.38	5.16	5.31	2.99	0.74
JT1.14	6.43	6.23	6.38	4.31	1.03
JT1.15	5.62	5.44	5.54	4.11	0.95
JT1.16	5.95	5.82	5.88	3.91	0.91
JT1.17	<0.014	<0.004	<0.016	<0.002	<0.001
JT1.18	15.96	15.47	15.76	5.83	1.78
JT1.19	3.28	3.21	3.23	0.04	0.01

Run 2:

Sample	165 -> 181 Ho	166 -> 182 Er	169 -> 185 Tm	172 -> 188 Yb	175 -> 191 Lu	178 -> 178 Hf	181 -> 181 Ta
JT2.1	0.41	1.12	0.15	0.99	0.15	3.20	0.31
JT2.2	0.13	0.40	0.06	0.42	0.06	1.73	0.17
JT2.3	0.36	0.96	0.14	0.87	0.13	3.00	0.28

Run 2:

Sample	182 -> 182 W	185 -> 185 Re	205 -> 205 Tl	206 -> 206 [Pb]	207 -> 207 [Pb]	208 -> 208 Pb	232 -> 232 Th
JT2.1	0.98	17.52	3.33	9.66	9.21	9.42	3.37
JT2.2	0.57	26.67	3.09	3.64	3.53	3.59	1.80
JT2.3	0.73	12.57	3.22	9.18	8.81	8.99	3.13

Sample	238 -> 238 U
JT2.1	0.72
JT2.2	0.37
JT2.3	0.69

APPENDIX C: DILUTION CALCULATIONS

Solution ICP-MS dilution calculations:

Sample	Sample wt (g)	HNO3 (g)	HNO3+sample(g)	DF (1)	Sample Aliquot (ml)	HNO3m(g) (2)	HNO3+sample(g)	DF (2)	DF (t)
JT1.1	0.1004	5.0560	5.1564	51.3663	0.2577	4.6298	4.8875	18.9669	974.2579
JT1.2	0.0994	5.0763	5.1757	52.0475	0.2544	4.6079	4.8622	19.1161	994.9460
JT1.3	0.1011	5.0691	5.1701	51.1489	0.2538	4.6284	4.8822	19.2365	983.9280
JT1.4	0.1016	5.0716	5.1731	50.9377	0.2540	4.6463	4.9004	19.2901	982.5930
JT1.5	0.0992	5.0716	5.1708	52.1360	0.2574	4.6356	4.8930	19.0063	990.9130
JT1.6	0.1028	5.0640	5.1668	50.2460	0.2487	4.6939	4.9427	19.8716	998.4700
JT1.7	0.1055	5.0694	5.1749	49.0457	0.2485	4.7049	4.9534	19.9327	977.6126
JT1.8	0.1150	5.0640	5.1790	45.0322	0.2503	4.6734	4.9236	19.6733	885.9318
JT1.9	0.1010	5.0662	5.1672	51.1564	0.2478	4.7040	4.9518	19.9844	1022.3319
JT1.10	0.1017	5.0587	5.1603	50.7608	0.2501	4.5655	4.8156	19.2527	977.2829
JT1.11	0.1013	5.0671	5.1684	51.0354	0.2518	4.7476	4.9994	19.8569	1013.4066
JT1.12	0.3016	5.0698	5.3714	17.8093	0.0912	4.8750	4.9662	54.4541	969.7903
JT1.13	0.1028	5.0670	5.1697	50.3097	0.2497	4.7267	4.9764	19.9319	1002.7678
JT1.14	0.1166	5.0480	5.1646	44.3081	0.2495	4.7018	4.9512	19.8477	879.4138
JT1.15	0.1005	5.0755	5.1760	51.5120	0.2487	4.7062	4.9549	19.9227	1026.2596
JT1.16	0.1039	5.0751	5.1791	49.8238	0.2492	4.6643	4.9135	19.7160	982.3266
JT1.17	0.0000	5.0677	5.0677	-	0.2456	4.6487	4.8942	19.9314	-
JT1.18	0.0994	5.0712	5.1706	52.0212	0.2492	4.7115	4.9607	19.9046	1035.4628
JT1.19	0.1241	5.0561	5.1802	41.7508	0.2534	4.7073	4.9608	19.5754	817.2914
JT2.1	0.1004	5.0000	5.1004	50.8241	0.3119	5.0902	5.4020	17.3218	880.3670
JT2.2	0.1070	5.0000	5.1070	47.7229	0.2540	5.0517	5.3056	20.8914	996.9974
JT2.3	0.1007	5.0000	5.1007	50.6490	0.2788	5.0468	5.3255	19.1050	967.6486

Raw solution ICP-MS data is normalised to the total dilution factor (DF(t)) of the sample and multiplied by 1000 to convert units to ppm.
Concentration (ppm) = ([ppb]*DF(t))/1000

APPENDIX D: MC-ICP-MS DATA

Neptune MC-ICP-MS raw isotope data.

Voltage		Analysis 1	Analysis 2	Analysis 3		
10V	NIST	0.44530	0.44530			
10V	JT1.1	0.44537	0.44537			
10V	NIST	0.44530	0.44530			
					d65Cu(ave)	**2sd**
	del	**0.166**	**0.160**	**#DIV/0!**	**0.16**	**0.008**

		Analysis 1	Analysis 2	Analysis 3		
10V	NIST	0.44530	0.44530			
12V	JT1.2	0.44540	0.44539			
10V	NIST	0.44530	0.44530			
					d65Cu(ave)	**2sd**
	del	**0.209**	**0.20798**	**#DIV/0!**	**0.21**	**0.001**

		Analysis 1	Analysis 2	Analysis 3		
8V	NIST	0.44531	0.44532			
8V	JT1.3	0.44551	0.44552			
8V	NIST	0.44532	0.44531			
					d65Cu(ave)	**2sd**
	del	**0.437**	**0.46163**	**#DIV/0!**	**0.45**	**0.035**

Voltage		Analysis 1	Analysis 2	Analysis 3		
8V	NIST	0.44531	0.44531			
8V	JT1.4	0.44527	0.44526			
8V	NIST	0.44531	0.44532			
					d65Cu(ave)	**2sd**
	del	**-0.098**	**-0.11464**	**#DIV/0!**	**-0.11**	**0.023**

		Analysis 1	Analysis 2	Analysis 3		
8V	NIST	0.44532	0.44532			
7V	JT1.5	0.44541	0.44541			
8V	NIST	0.44532	0.44533			
					d65Cu(ave)	**2sd**
	del	**0.210**	**0.20705**	**#DIV/0!**	**0.21**	**0.005**

		Analysis 1	Analysis 2	Analysis 3		
8V	NIST	0.44533	0.44531			
9V	JT1.6	0.44555	0.44554			
8V	NIST	0.44531	0.44532			
					d65Cu(ave)	**2sd**
	del	**0.51634**	**0.50918**	**#DIV/0!**	**0.51**	**0.010**

		Analysis 1	Analysis 2	Analysis 3		
8V	NIST	0.44532	0.44532			
8V	JT1.7	0.44559	0.44558			
8V	NIST	0.44532	0.44531			
					d65Cu(ave)	**2sd**
	del	**0.59644**	**0.58900**	**#DIV/0!**	**0.59**	**0.011**

Voltage		Analysis 1	Analysis 2	Analysis 3		
8V	NIST	0.44531	0.44532			
10V	JT1.8	0.44545	0.44543			
8V	NIST	0.44532	0.44531			
					d65Cu(ave)	**2sd**
	del	**0.29378**	**0.27721**	**#DIV/0!**	**0.29**	**0.023**

		Analysis 1	Analysis 2	Analysis 3		
8V	NIST	0.44531	0.44532			
9V	JT1.9	0.44535	0.44536			
8V	NIST	0.44532	0.44531			
					d65Cu(ave)	**2sd**
	del	**0.08017**	**0.10235**	**#DIV/0!**	**0.091**	**0.031**

		Analysis 1	Analysis 2	Analysis 3		
8V	NIST	0.44531	0.44531			
10V	JT1.10	0.44546	0.44546			
8V	NIST	0.44531	0.44532			
					d65Cu(ave)	**2sd**
	del	**0.32364**	**0.32806**	**#DIV/0!**	**0.33**	**0.006**

		Analysis 1	Analysis 2	Analysis 3		
8V	NIST	0.44532	0.44530			
8V	JT1.11	0.44550	0.44551			
8V	NIST	0.44530	0.44532			
					d65Cu(ave)	**2sd**
	del	**0.41943**	**0.44474**	**#DIV/0!**	**0.43**	**0.036**

Voltage		Analysis 1	Analysis 2	Analysis 3		
	NIST	0.44536	0.44536	0.44537		
7.1	JT1.12	0.44540	0.44542	0.44542		
	NIST	0.44536	0.44535	0.44537		
					d65Cu(ave)	**2sd**
	del	**0.09544**	**0.14058**	**0.11325**	**0.11643**	**0.04548**

		Analysis 1	Analysis 2	Analysis 3		
	NIST	0.44535	0.44536			
6.6	JT1.13	0.44551	0.44552			
	NIST	0.44536	0.44536			
					d65Cu(ave)	**2sd**
	del	**0.36467**	**0.36685**	**#DIV/0!**	**0.36576**	**0.00309**

		Analysis 1	Analysis 2	Analysis 3		
	NIST	0.44536	0.44536			
6.0	JT1.14	0.44548	0.44548			
	NIST	0.44536	0.44536			
					d65Cu(ave)	**2sd**
	del	**0.26985**	**0.27262**	**#DIV/0!**	**0.27124**	**0.00392**

		Analysis 1	Analysis 2	Analysis 3		
	NIST	0.44536	0.44536			
8.8	JT1.15	0.44550	0.44550			
	NIST	0.44536	0.44536			
					d65Cu(ave)	**2sd**
	del	**0.30999**	**0.32353**	**#DIV/0!**	**0.31676**	**0.01915**

Voltage		Analysis 1	Analysis 2	Analysis 3		
	NIST	0.44536	0.44536			
5.8	JT1.16	0.44547	0.44545			
	NIST	0.44536	0.44535			
					d65Cu(ave)	**2sd**
	del	**0.23718**	**0.20260**	**#DIV/0!**	**0.21989**	**0.04890**

		Analysis 1	Analysis 2	Analysis 3		
	NIST	0.44535	0.44537			
10.0	JT1.18 AGV-2	0.44535	0.44542			
	NIST	0.44535	0.44537			
					d65Cu(ave)	**2sd**
	del	**-0.00731**	**0.11325**	**#DIV/0!**	**0.05297**	**0.17050**

		Analysis 1	Analysis 2	Analysis 3	Analysis 4		
10V	NIST	0.44530	0.44529	0.44532	0.44543		
8V	JT1.19 BIR-1	0.44530	0.44531	0.44534	0.44542		
	NIST	0.44529	0.44530	0.44532	0.44540		
						d65Cu(ave)	**2sd**
	del	**0.010**	**0.031**	**0.057**	**0.01337**	**0.03**	**0.043**

		Analysis 1	Analysis 2	Analysis 3		
	NIST	0.44535	0.44535			
9.9	JT2.1	0.44546	0.44545			
	NIST	0.44535	0.44535			
					d65Cu(ave)	**2sd**
	del	**0.24672**	**0.22719**	**#DIV/0!**	**0.23695**	**0.02761**

Voltage		Analysis 1	Analysis 2	Analysis 3		
	NIST	0.44536	0.44536			
6.7	JT2.3	0.44554	0.44554			
	NIST	0.44536	0.44536			
					d65Cu(ave)	**2sd**
	del	**0.40090**	**0.39949**	**#DIV/0!**	**0.400**	**0.002**

		Analysis 1	Analysis 2	Analysis 3		
	NIST	0.44535	0.44535			
8.1	JT2.2	0.44552	0.44551			
	NIST	0.44535	0.44536			
					d65Cu(ave)	**2sd**
	del	**0.37132**	**0.33329**	**#DIV/0!**	**0.35231**	**0.05378**

APPENDIX E: PETROGRAPHY

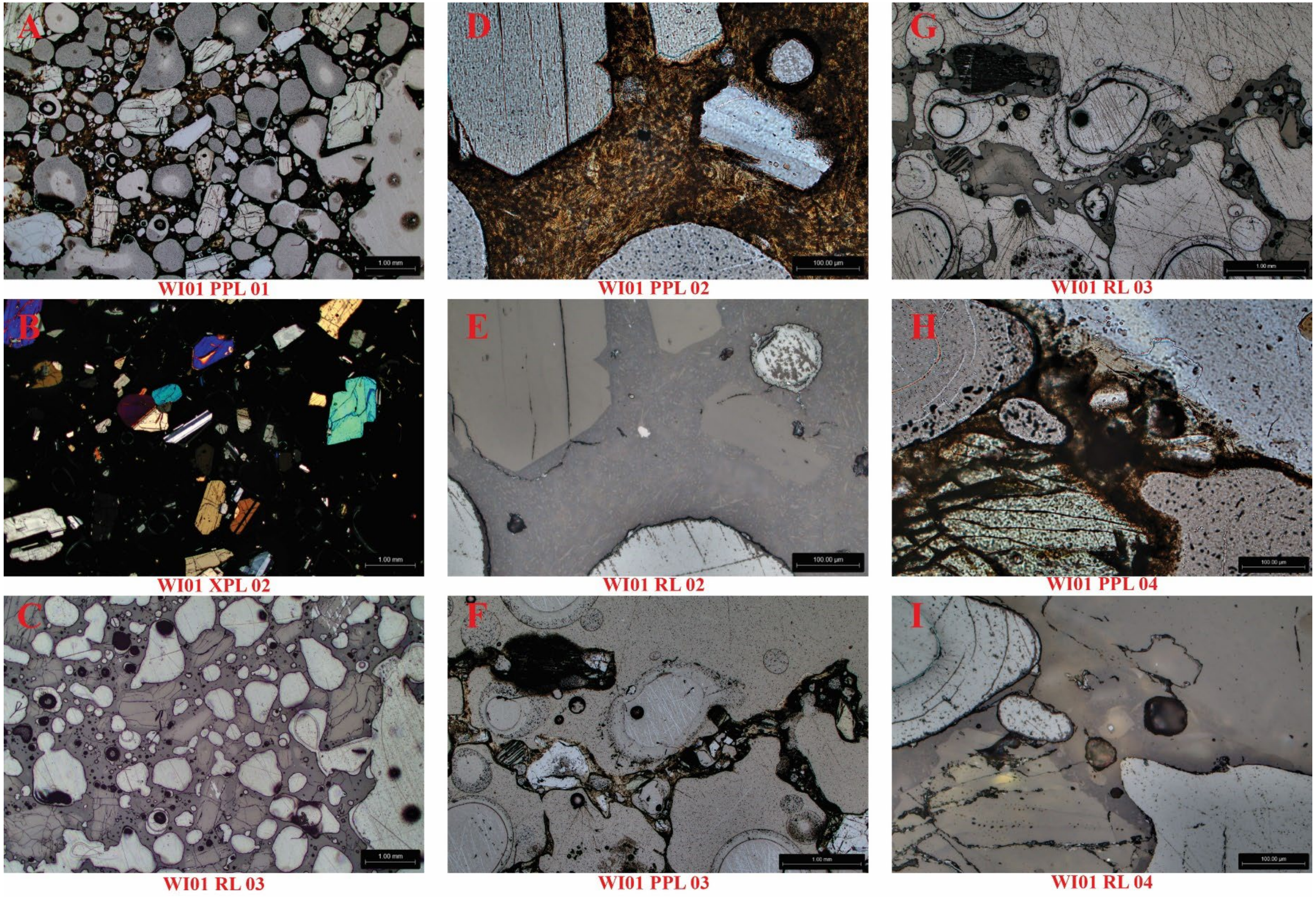

WI01 PPL 01

WI01 XPL 02

WI01 RL 03

WI01 PPL 02

WI01 RL 02

WI01 PPL 03

WI01 RL 03

WI01 PPL 04

WI01 RL 04

Figure 1: Petrography of sample WI01

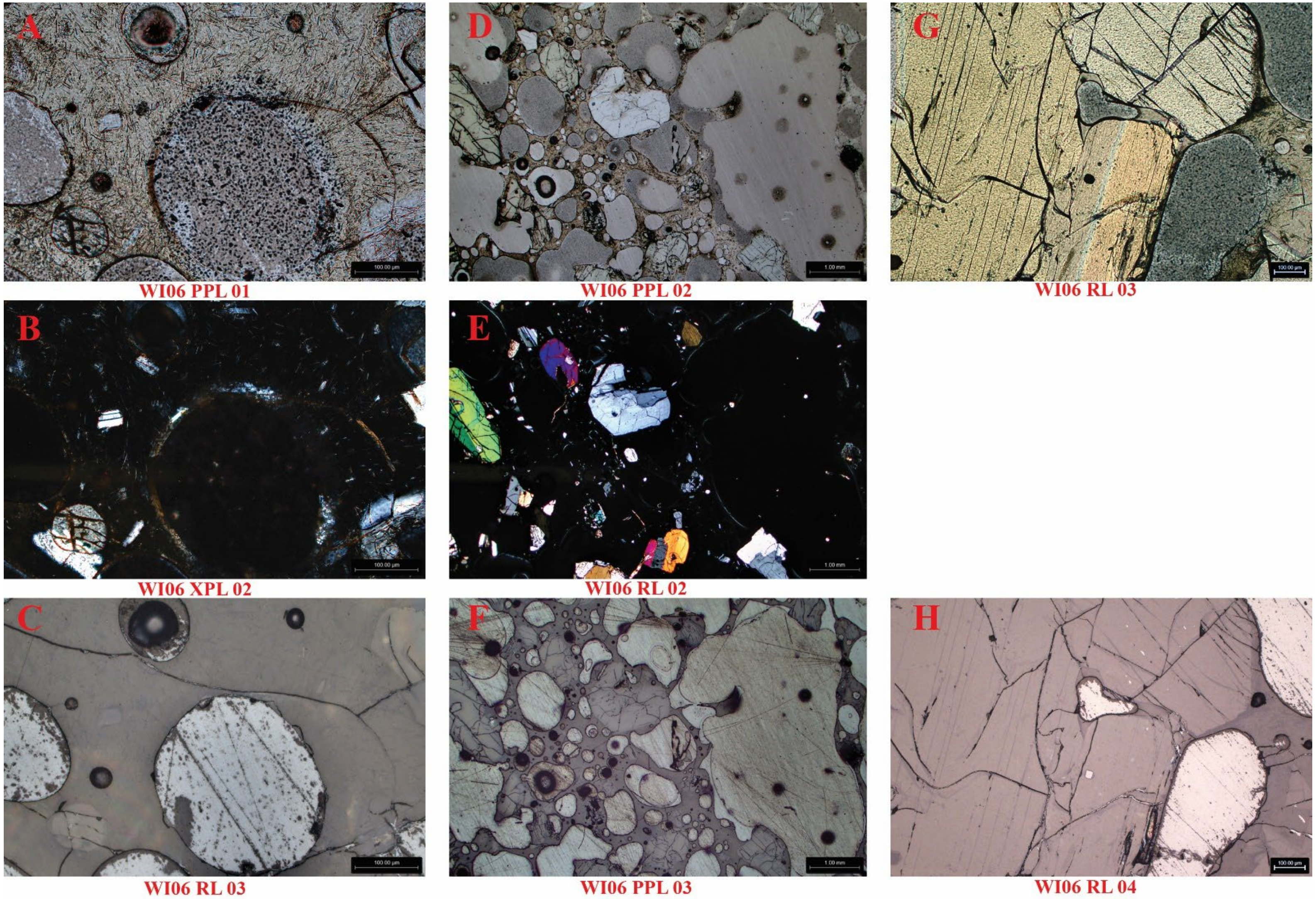

WI06 PPL 01

WI06 PPL 02

WI06 RL 03

WI06 XPL 02

WI06 RL 02

WI06 RL 03

WI06 PPL 03

WI06 RL 04

Figure 2: Petrography of sample WI06. Top: Plain polarised light. Middle: Cross polarised light. Bottom: Reflected light

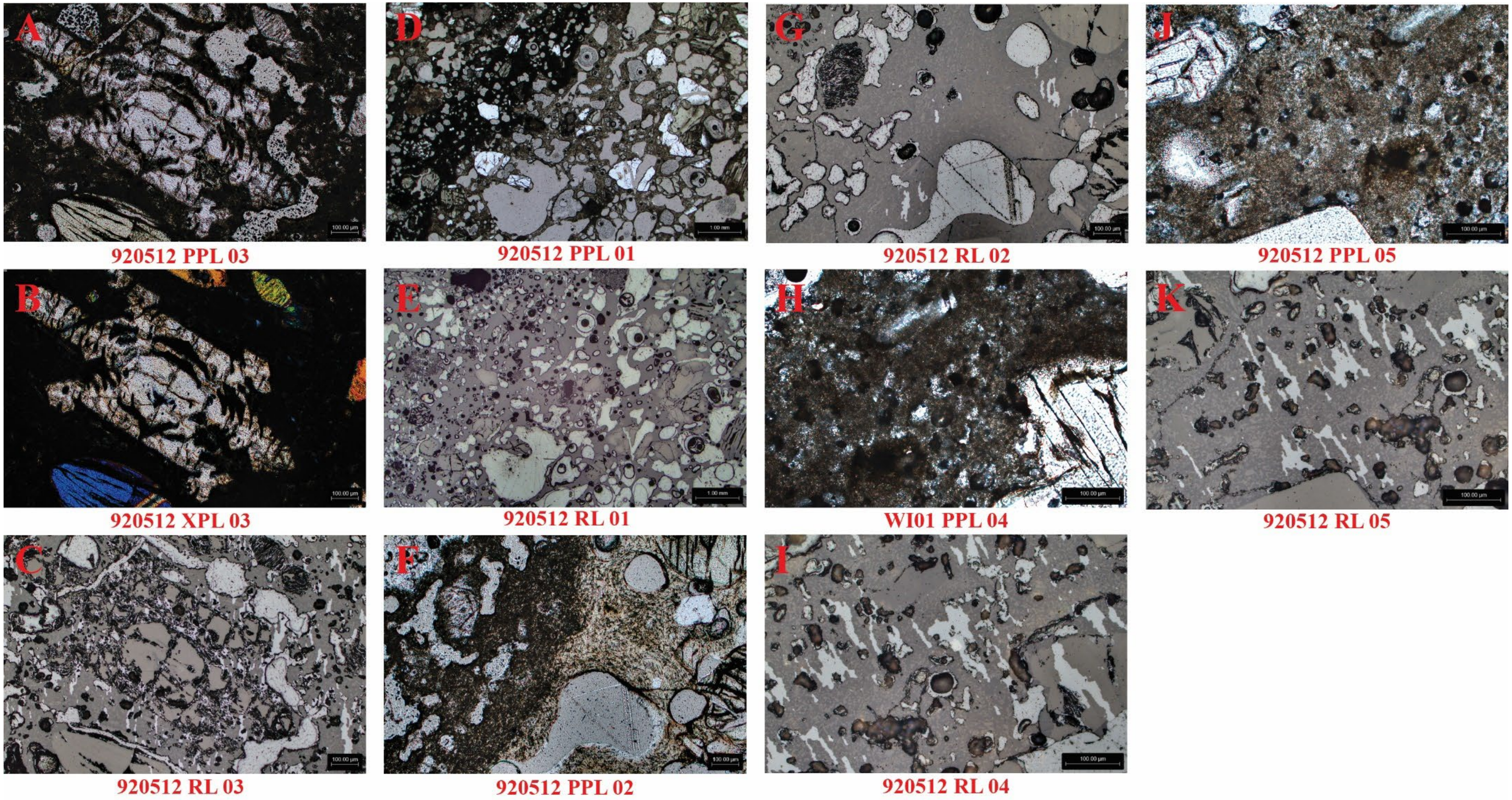

920512 PPL 03

920512 XPL 03

920512 RL 03

920512 PPL 01

920512 RL 01

920512 PPL 02

920512 RL 02

WI01 PPL 04

920512 RL 04

920512 PPL 05

920512 RL 05

Figure 3: Petrography of sample 920512

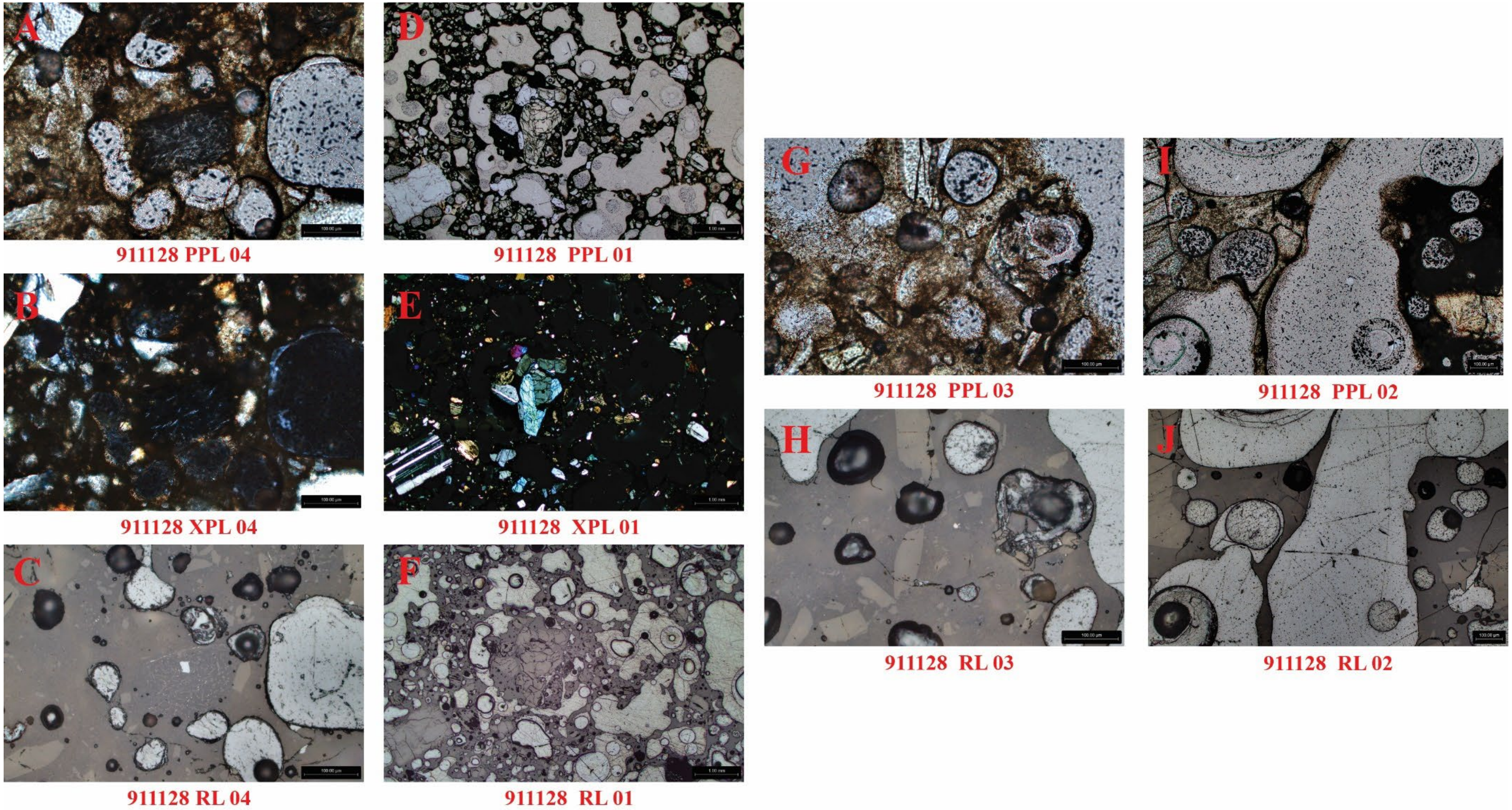

911128 PPL 04

911128 XPL 04

911128 RL 04

911128 PPL 01

911128 XPL 01

911128 RL 01

911128 PPL 03

911128 RL 03

911128 PPL 02

911128 RL 02

Figure 4: Petrography of sample 911128

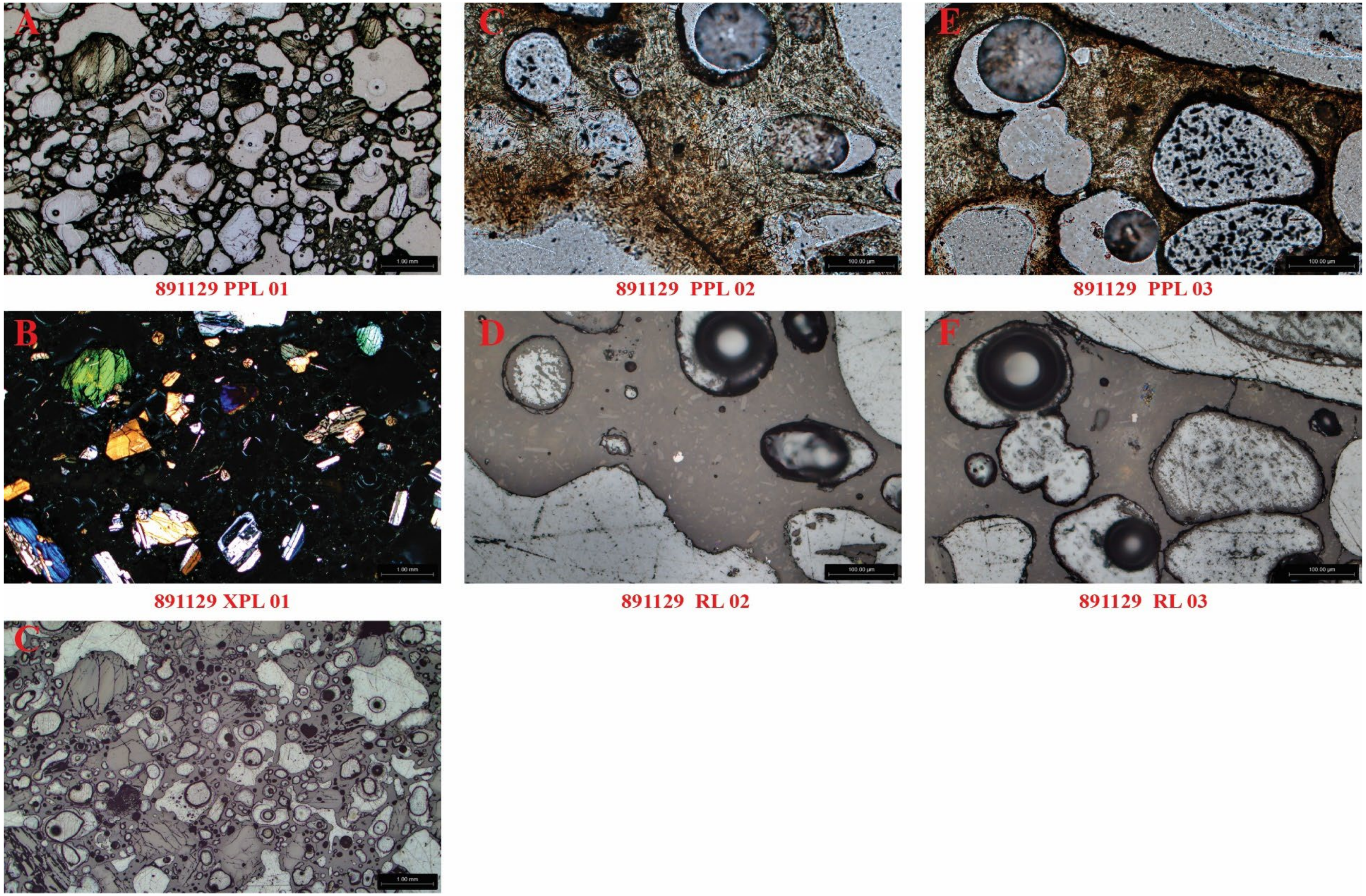

891129 PPL 01

891129 PPL 02

891129 PPL 03

891129 XPL 01

891129 RL 02

891129 RL 03

891129RL 01

Figure 5: Petrography of sample 891129

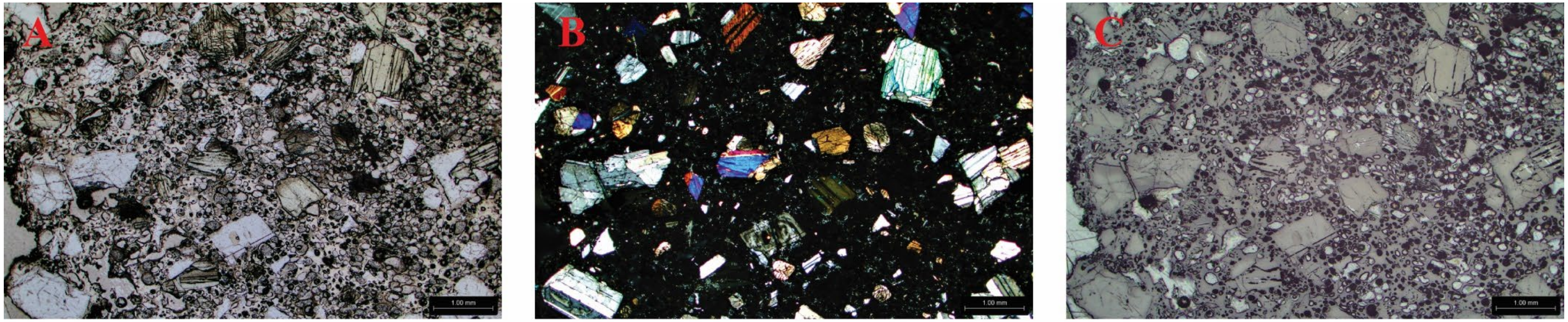

820210 PPL 01

820210 XPL 01

820210 RL 01

Figure 6: Petrography of sample 820210

APPENDIX F: USGS STANDARD ERRORS

Solution ICP-MS USGS standard error percentages.

Red = >10%

Blue = >-10%

Standard	B	Ba	Be	Cd	Ce	Co	Co	Cr	Cs	Cu	Dy	Er	Eu	Ga	Ga	Ga	Gd	Ge
AGV-2	######	5.9	18.2	-35.8	-3.6	9.6	3.2	10.1	6.5	-1.5	-5.7	-2.4	-6.1	406.2	4.0	10.4	-5.9	######
BIR-1a	######	-9.3	-14.3	######	-10.8	6.6	-0.6	13.0	######	-0.8	-5.3	-4.8	-6.3	-0.6	3.3	2.1	-2.6	######

Standard	Ge	Hf	Hf	Ho	La	Li	Lu	Mn	Mo	Mo	Nb	Nd	Ni	Ni	P	Pb	Pb	Pb
AGV-2	######	-1.3	0.8	-3.9	-2.3	25.2	-6.7	######	5.9	19.5	-13.0	-2.9	1.8	0.1	######	61.7	21.9	24.2
BIR-1a	######	-2.0	-0.9	-7.5	-10.2	10.9	-10.5	######	-49.5	######	-5.7	-9.1	5.5	5.8	######	426.1	-13.7	-13.0

Standard	Pr	Rb	S	S	Sc	Sm	Sn	Sn	Sn	Sr	Ta	Ta	Tb	Th	Ti	Ti	Tl
AGV-2	-4.5	8.2	#DIV/0!	######	-36.3	437.2	20.1	26.6	19.7	10.8	-4.1	-12.0	-11.1	-2.3	######	#DIV/0!	-8.5
BIR-1a	-11.1	-53.3	#DIV/0!	######	-45.8	95.7	-1.8	1.0	-2.1	-2.3	385.6	233.6	-8.4	-10.3	######	#DIV/0!	######

Standard	Tm	U	V	W	Y	Yb	Zn	Zr
AGV-2	-6.0	-2.4	-0.5	263.6	-8.3	-7.9	7.4	8.7
BIR-1a	-10.9	-14.5	21.3	5112.5	-17.1	-7.4	10.8	-10.3